

DYNAMICS OF THE GLOBULAR CLUSTER SYSTEM ASSOCIATED WITH
M87 (NGC 4486). II. ANALYSIS

PATRICK CÔTÉ,^{1,2,3,4} DEAN E. MCLAUGHLIN,^{4,5,6} DAVID A. HANES,^{4,7,8,9} TERRY J. BRIDGES,^{4,8,10,11} DOUG GEISLER,^{12,13,14}
DAVID MERRITT,² JAMES E. HESSER,⁹ GRETCHEN L. H. HARRIS,¹⁵ AND MYUNG GYOON LEE¹⁶

Received 2001 March 9; accepted 2001 June 6

ABSTRACT

We present a dynamical analysis of the globular cluster system associated with M87 (=NGC 4486), the cD galaxy near the dynamical center of the Virgo Cluster. The analysis utilizes a new spectroscopic and photometric database, which is described in a companion paper. Using a sample of 278 globular clusters with measured radial velocities and metallicities and new surface density profiles based on wide-field Washington photometry, we study the dynamics of the M87 globular cluster system both globally (for the entire cluster sample) and separately (for the metal-rich and metal-poor globular cluster samples). This constitutes the largest sample of radial velocities for pure Population II tracers yet assembled for any external galaxy. Our principal findings are summarized as follows:

1. Surface density profiles constructed from our Washington photometry reveal the metal-poor cluster system to be more spatially extended than its metal-rich counterpart, consistent with earlier findings based on *Hubble Space Telescope* imaging in the central regions of the galaxy. Beyond a radius of $R \simeq 1.5R_e$ (10 kpc), the metal-poor component dominates the total globular cluster system.

2. When considered in their entirety, each of the combined, metal-poor and metal-rich globular cluster samples (278, 161, and 117 clusters, respectively) appears to rotate, with similar rotation amplitudes, about axes whose position angles are indistinguishable from that of the photometric minor axis, $\Theta_0 = 65^\circ$.

3. The one-dimensional rotation curve (i.e., binned in circular annuli) for the metal-rich cluster system has a roughly constant mean amplitude of $\Omega R = 160_{-99}^{+120}$ km s⁻¹. The metal-rich clusters appear to be rotating, at all radii, about the photometric minor axis of the galaxy. However, a smoothed, two-dimensional map of the line-of-sight velocity residuals reveals the rotation field for the metal-rich clusters to be noncylindrical in nature. Instead, it exhibits a “double-lobed” pattern, with maxima at $R \sim 3.5R_e - 4R_e$ (25–30 kpc) along the approximate photometric major axis of the galaxy.

4. The one-dimensional rotation curve of the metal-poor cluster system has mean amplitude of $\Omega R = 172_{-108}^{+51}$ km s⁻¹. The two-dimensional map of the rotation field for the metal-poor clusters shows some evidence for solid-body rotation or, alternatively, for a “shear” in the line-of-sight velocity. This shear is similar in size and orientation to that observed for Virgo galaxies within 2° of M87 and is consistent with a scenario, previously suggested on the basis of dwarf galaxy kinematics and X-ray imaging, in which material is gradually infalling onto M87 along the so-called principal axis of the Virgo Cluster.

5. Beyond a radius of $R \simeq 2R_e$ (15 kpc), the approximate onset of the galaxy’s cD envelope, the metal-poor globular cluster system rotates about the photometric minor axis, similar to its metal-rich counterpart. Inside this radius, however, the metal-poor clusters appear to rotate around the photometric major axis.

6. The complete sample of 278 globular clusters has an almost perfectly isotropic velocity ellipsoid, with $\beta_{c1} = 1 - \sigma_\theta^2/\sigma_r^2 \simeq 0$.

¹ California Institute of Technology, Mail Stop 105-24, Pasadena, CA 91125.

² Department of Physics and Astronomy, Rutgers University, New Brunswick, NJ 08854.

³ Sherman M. Fairchild Fellow.

⁴ Visiting Astronomer, Canada-France-Hawaii Telescope, operated by the National Research Council of Canada, the Centre National de la Recherche Scientifique of France, and the University of Hawaii.

⁵ Department of Astronomy, 601 Campbell Hall, University of California, Berkeley, Berkeley, CA 94720-3411.

⁶ Hubble Fellow.

⁷ Department of Physics, Queen’s University, Kingston, ON K7L 3N6, Canada.

⁸ Anglo-Australian Observatory, P.O. Box 296, Epping, NSW, 1710, Australia.

⁹ Dominion Astrophysical Observatory, Herzberg Institute of Astrophysics, National Research Council, 5071 West Saanich Road, Victoria, BC V8W 3P6, Canada.

¹⁰ Royal Greenwich Observatory, Madingley Road, Cambridge, CB3 0EZ, UK.

¹¹ Institute of Astronomy, Madingley Road, Cambridge, CB3 0HA, UK.

¹² Physics Department, Astronomy Group, University of Concepcion, Casilla 160-C, Concepcion, Chile.

¹³ Visiting Astronomer, Cerro Tololo Inter-American Observatory, which is operated by AURA, Inc., under cooperative agreement with the National Science Foundation.

¹⁴ Visiting Astronomer, Kitt Peak National Observatory, which is operated by AURA, Inc., under cooperative agreement with the National Science Foundation.

¹⁵ Department of Physics, University of Waterloo, Waterloo, ON N2L 3G1, Canada.

¹⁶ Astronomy Program, SEES, Seoul National University, Seoul 151-742, Korea.

7. When considered separately, the metal-poor cluster system shows a modest but significant tangential bias of $\beta_{cl} \simeq -0.4$, while the velocity ellipsoid of the metal-rich cluster system is radially biased, with $\beta_{cl} \simeq 0.4$.

Taken together, these results demonstrate that the dual nature of the M87 globular cluster system, first identified on the basis of its bimodal metallicity distribution, also extends to its dynamical properties. We discuss the implications of these findings for the various formation scenarios proposed for giant elliptical galaxies and their globular cluster systems.

Subject headings: galaxies: clusters: general — galaxies: halos — galaxies: individual (M87) — galaxies: kinematics and dynamics — galaxies: star clusters

1. INTRODUCTION

As surviving relics from the epoch of galaxy formation, globular clusters (GCs) provide important insights into the processes that shaped their present-day host galaxies. The observed properties of GCs in giant elliptical galaxies, such as their total numbers, chemical abundances, and spatial distributions, have been used alternatively to argue for a wide diversity of formation processes, including dissipative (monolithic) collapse, spiral-spiral mergers (Ashman & Zepf 1992), multimodal star formation histories caused by galactic winds (Harris, Harris, & McLaughlin 1998), and dissipationless hierarchical growth (Côté, Marzke, & West 1998; Côté et al. 2000). There is, however, one important piece of observational evidence that has been almost entirely absent in such discussions: the dynamical properties of the GCs. Because of the faintness of even the most luminous GCs in nearby giant elliptical galaxies, the requisite spectroscopic observations are extremely challenging, and it is only recently that radial velocities for significant samples of clusters have been accumulated in a handful of galaxies (e.g., Cohen & Ryzhov 1997; Sharples et al. 1998; Zepf et al. 2000).

M87, the incipient cD galaxy near the dynamical center of the Virgo Cluster, offers an ideal testing ground for the various formation scenarios. It has by far the most populous globular cluster system (GCS) of any nearby galaxy (e.g., $N_{cl} \simeq 13,500$; McLaughlin, Harris, & Hanes 1994), and a wealth of observational data has been accumulated for both the galaxy itself and the surrounding Virgo Cluster. Such material includes numerous analyses of the photometric properties and spatial distribution of M87 GCs (e.g., Strom et al. 1981; McLaughlin et al. 1994; D. Geisler, M. G. Lee, & E. Kim 2001, in preparation), surface brightness profiles for the galaxy light (de Vaucouleurs & Nieto 1978; Carter & Dixon 1978), stellar dynamical studies of the central regions of M87 (van der Marel 1994), photometric and radial velocity surveys of surrounding Virgo Cluster galaxies (Binggeli, Sandage, & Tammann 1985; Binggeli, Popescu, & Tammann 1993; Girardi et al. 1996), and X-ray observations of the hot intracluster gas that fills the Virgo gravitational potential well (Nulsen & Böhringer 1995).

The dynamics of the M87 GCS has been addressed in several previous studies, albeit in varying levels of detail. Early efforts (Huchra & Brodie 1987; Mould, Oke, & Nemeč 1987; Mould et al. 1990) were hampered by limited sample sizes: for example, the compilation of Mould et al. (1990) consisted of radial velocities for only 43 clusters. Although these data were sufficient to provide a provisional mass estimate for M87 and to hint at the presence of rotation in the GCS, it was shown by Merritt & Tremblay (1993) that this sample provides only weak constraints on the distribution of dark matter in the M87 halo. Moreover, Merritt & Tremblay (1993) demonstrated that a measure-

ment of the velocity anisotropy of GCS would require radial velocities for a minimum sample of several hundred clusters.

In a major observational effort, Cohen & Ryzhov (1997) used the Keck telescope to measure radial velocities for a total of 205 GCs surrounding M87. Using these data, Cohen & Ryzhov (1997) found clear evidence for a rising velocity dispersion profile and derived a total mass of $M = (3.8 \pm 1.2) \times 10^{12} M_{\odot}$ within a volume of radius $r \simeq 33$ kpc centered on M87. An independent analysis of these velocities by Kissler-Patig & Gebhardt (1998) suggested that the M87 GCS is rotating rapidly at large radii, i.e., $\Omega R \simeq 300 \text{ km s}^{-1}$ beyond a projected radius of $R = 3R_e$ (20 kpc).¹⁷ This rapid rotation was subsequently confirmed by Cohen (2000), who augmented her original radial velocity sample to include 17 additional clusters having $R \geq 3R_e$.

While the amount of angular momentum implied by these results is large, there is emerging evidence from radial velocity surveys of planetary nebulae that giant elliptical galaxies may, as a class, rotate rapidly at large radii (e.g., Hui et al. 1995; Arnaboldi et al. 1996, 1998). An enormous amount of theoretical effort has been devoted to understanding the acquisition of angular momentum during galaxy formation, e.g., via tidal torques in monolithic collapse scenarios (Peebles 1969), or through the conversion of orbital and spin angular momentum of the progenitor galaxies in major (Heyl, Hernquist, & Spergel 1996) and multiple (Weil & Hernquist 1996) mergers. The angular momentum content of elliptical galaxies may thus constitute an important clue to their formation; ultimately, the rotation properties of the chemically distinct GC populations in these galaxies may provide a powerful means of discriminating between the various formation models described above.

In this paper we present a dynamical analysis of the M87 GCS using an improved and expanded sample of radial velocities. In addition, new Washington CT_1 photometry is used to derive metallicities for all program objects and to investigate correlations between metallicity and dynamics by carrying out separate analyses for both the metal-rich and metal-poor GC populations.

2. THE DATABASE

The database used in the analysis presented below is a subset of that which has been described in detail in a companion paper (Hanes et al. 2001, hereafter Paper I), so only a brief summary is given here. The reader is referred to Paper I for a complete description of the sample properties, observational material, and data reductions.

¹⁷ According to de Vaucouleurs & Nieto (1978), $R_e = 96''$ for M87. Throughout this paper we adopt an M87 distance of $D = 15$ Mpc (Pierce et al. 1994; Ferrarese et al. 1996), so that $1' = 4.364$ kpc.

2.1. Photometry and Radial Velocities

One of our goals is to investigate the relationship between GC dynamics and metallicity, so we require homogeneous metallicity estimates for our sample of clusters. Such information is most easily obtained from broadband photometry. Unfortunately, although there have been numerous photometric studies of the M87 GCs, the large areal coverage of our radial velocity survey means that no single existing survey includes all of our program objects. For instance, the most extensive published photometric survey of the M87 GCS remains that of Strom et al. (1981), who presented photographic *UBR* photometry for 1728 candidate GCs surrounding M87. However, our sample includes many objects not included in the Strom et al. (1981) catalog, e.g., objects that are at large radii, beyond the limits of their survey, or close to the galaxy center where crowding and background contamination are severe. Therefore, as described in Paper I, we have obtained deep, wide-field CCD images centered on M87 using the CTIO and KPNO 4 m telescope. Imaging was carried out in Washington *C* and T_1 filters, since the long color baseline of the $C - T_1$ index provides exceptional metallicity sensitivity (see, e.g., Geisler, Lee, & Kim 1996). The photometric observations, calibrations, and reductions have been described briefly in Paper I, while a more comprehensive description of the photometric properties of the M87 GCS based on these data will be presented in a forthcoming paper (D. Geisler et al. 2001, in preparation).

The sample of radial velocities we begin with here consists of data for 334 candidate and previously confirmed GCs. This number includes 145 measurements from the Canada-France-Hawaii Telescope (CFHT), 87 of which are for targets not observed in any of the previous surveys of Huchra & Brodie (1987), Mould et al. (1987, 1990), Cohen & Ryzhov (1997), or Cohen (2000). The total is down slightly from the full database of 352 objects in Paper I, as we have discarded out of hand 12 targets for which we were unable to obtain unambiguous Washington photometry (IDs 881, 5053, 5055, 5058, 5064, 5065, 5066, 5067, 5071, 9002, 9051, and 9052 from Paper I), five that were already identified by Cohen & Ryzhov (1997) as Galactic M stars (IDs 38, 87, 782, 1551, 8001), and one object that turns out to be visibly nonstellar (ID 207).

All measurements have been transformed onto common astrometric and radial velocity scales. We adopt the radial velocity and uncertainty from our own analysis for all targets observed at the CFHT and transform all other data to this system as described in Paper I. Briefly, cluster candidates that were not observed at the CFHT, but were observed at Keck by Cohen & Ryzhov (1997), are transformed onto our Multi-Object Spectrograph (MOS) velocity scale according to

$$v_p(\text{MOS}) = 0.96v_p(\text{CR97}) + 91$$

and assigned an uncertainty of $\pm 100 \text{ km s}^{-1}$, as recommended by these authors.¹⁸ Objects measured neither by us nor by Cohen & Ryzhov (1997), but by Cohen (2000), are transformed as

$$v_p(\text{MOS}) = 0.98v_p(\text{C2000}) + 120$$

and given an uncertainty of $\pm 50 \text{ km s}^{-1}$. Finally, to targets with velocities recorded only by Mould et al. (1987) or Mould et al. (1990), we apply the correction

$$v_p(\text{MOS}) = 0.76v_p(\text{Mould}) + 280$$

and adopt an uncertainty of $\pm 200 \text{ km s}^{-1}$.

2.2. Sample Selection

Before proceeding with the dynamical analysis, it is important first to identify a sample of bona fide M87 GCs. Culling Galactic field stars from the sample on the basis of radial velocity is not trivial since the relatively low systemic velocity of M87 ($1277 \pm 2 \text{ km s}^{-1}$; van der Marel 1994) and the high velocity dispersion of the GCS (i.e., $\langle \sigma_p \rangle \sim 400 \text{ km s}^{-1}$; see § 3) make the correct choice of the low-velocity cutoff problematic. We adopted a selection criterion of

$$200 \leq v_p \leq 2550 \text{ km s}^{-1}. \quad (1)$$

This range is roughly symmetric about the mean velocity, $\langle v_p \rangle = 1350 \text{ km s}^{-1}$, of the M87 GCS (see § 3) and is expected to exclude the vast majority of foreground stars and background galaxies. We also imposed a selection on $C - T_1$ color, discarding all objects that did not have colors within the range

$$0.8 \leq C - T_1 \leq 2.35 \text{ mag}. \quad (2)$$

The Galactic foreground extinction in the direction of M87, according to the DIRBE maps of Schlegel, Finkbeiner, & Davis (1998), is $E(B - V) = 0.022 \text{ mag}$, which corresponds to $E(C - T_1) = 0.045 \text{ mag}$ (Secker et al. 1995). The metallicity calibration of Geisler & Forte (1990) suggests that this color selection will confine our sample to clusters having metallicities in the range $-2.6 \leq [\text{Fe}/\text{H}] \leq 1.0 \text{ dex}$, an interval that should encompass virtually all GCs in M87 (e.g., Cohen, Blakeslee, & Ryzhov 1998). These selection criteria are illustrated in the upper panels of Figure 1. The filled histograms in these two panels show the color and velocity distributions for all 334 candidate GCs with measured radial velocities and $(C - T_1)$ colors. The dashed vertical lines in each panel show the adopted upper and lower selection limits. The dotted vertical line in the upper left panel shows our adopted dividing point between the metal-rich and metal-poor cluster populations: $C - T_1 = 1.42$. This color, which corresponds to a metallicity of $[\text{Fe}/\text{H}] = -1.16 \text{ dex}$, was chosen based on the observed dip in the $(C - T_1)$ distribution of the 2744 GC candidates from the photometric catalog of D. Geisler et al. (2001, in preparation) that have $T_1 \leq 22$ (*dashed histogram*).

The lower panel of Figure 1 is a color-velocity diagram for these same objects. The dotted region shows the joint selection criteria on color and velocity, which together identify a total of 278 bona fide GCs. Of these, 161 are classified as “blue” ($C - T_1 < 1.42$), or metal-poor, and 117 are considered “red” ($C - T_1 > 1.42$), or metal-rich, for purposes of the analysis and modeling in §§ 3 and 4. Note that three objects (IDs 161, 508, and 1602) have radial velocities that are appropriate for M87 GCs and yet have $C - T_1$ colors that are far too red for true clusters (i.e., the inferred metallicities are typically several hundred times above solar). A fourth candidate (ID 5002) has a radial velocity near the mean of the GC sample but an anomalously blue color. Although we have no reason to suspect either the colors or the velocities of these objects, their nature is unclear and additional observations are clearly warranted, first and

¹⁸ Here and throughout, quantities referred to the line of sight are denoted by a subscript *p*.

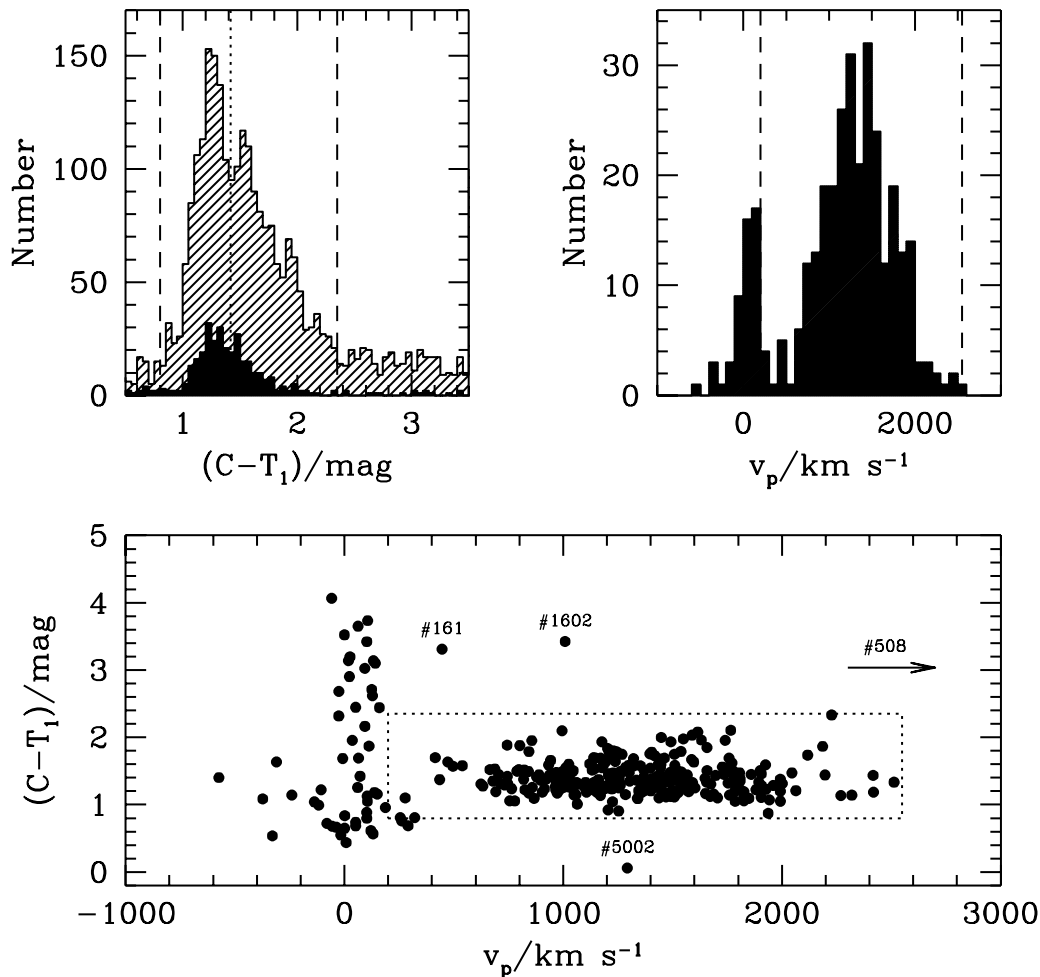


FIG. 1.—*Upper Left Panel*: Distribution of $(C-T_1)$ colors for 334 GC candidates with measured radial velocities (*solid histogram*). For comparison, the color distribution of all 2744 GC candidates from the photometric study of D. Geisler et al. (2001, in preparation) is shown as the dashed histogram. The dashed vertical lines indicate our adopted selection criteria on color, $0.80 \leq (C-T_1) \leq 2.35$ mag, while the dotted vertical line shows the color, $(C-T_1) = 1.42$, used to isolate the blue and red cluster samples. *Upper Right Panel*: Radial velocity histogram for the 334 candidate GCs with accurate $(C-T_1)$ colors. The vertical lines show our adopted selection criteria on velocity: $200 \leq v \leq 2550$ km s⁻¹. *Lower Panel*: Color vs. radial velocity for our initial sample of 334 objects. The dotted region shows the joint selection criteria on color and radial velocity. This box defines a final sample of 278 bona fide GCs.

foremost to confirm our results (particularly for Strom 508, an unresolved object that has a high radial velocity of $v_p = 5817 \pm 120$ km s⁻¹ but a very red color of $C-T_1 \approx 3.0$). In any event, all four are omitted from the following analysis.

Our innermost GC is projected to a distance of roughly 36" from the center of M87 (or about 2.6 kpc for our assumed distance of 15 Mpc to the galaxy), while the outermost member of our sample lies at $R \approx 631'' \approx 46$ kpc. Figure 2 shows the distribution on the sky of all 278 bona fide GCs (i.e., those objects falling inside the dotted region in the lower panel of Figure 1). The filled circles on this plot denote 109 clusters that were observed by us at the CFHT; of these, 54 are entirely new measurements and the rest are repeat observations of GCs identified in one of the earlier studies. The open symbols refer to data taken from these other surveys, as indicated in the legend. The straight line running through the figure represents the photometric major axis of the M87 halo light (oriented at 155° east of north; Carter & Dixon 1978), the inner circle marks the effective radius of the galaxy light ($R_e = 96'' \approx 7$ kpc; de Vaucouleurs & Nieto 1978), and the larger, dashed circle has a radius of $414'' \approx 30$ kpc $\approx 4.3R_e$. Outside this circle, the azimuthal coverage of the composite radial velocity database is far from complete, a situation that can signifi-

cantly compromise any inferences on the kinematics of the GCS at such large galactocentric distances (see below).

3. KINEMATICS OF THE CLUSTER SYSTEM

In previous analyses of the kinematics of the M87 GCS, investigators have usually proceeded by fitting sine curves to their line-of-sight velocities, v_p , as a function of projected azimuth, Θ , in order to test for the presence of rotation and to measure its amplitude (see Cohen & Ryzhov 1997; Kissler-Patig & Gebhardt 1998; Cohen 2000). We shall do the same here, but we pause first to clarify precisely what this assumes about the intrinsic velocity field of the GCS.

3.1. Mathematical Context

Consider a spherical GCS rotating about some axis, with an angular velocity ω that may be any axisymmetric function of position inside the galaxy.¹⁹ Let r , θ , and ϕ denote the usual spherical coordinate system within the GCS, such

¹⁹ While it is clearly imperfect (see, e.g., McLaughlin, Harris, & Hanes 1994), the assumption of spherical symmetry in the M87 GCS is not grossly in error, and we invoke it as a simplifying approximation throughout this paper.

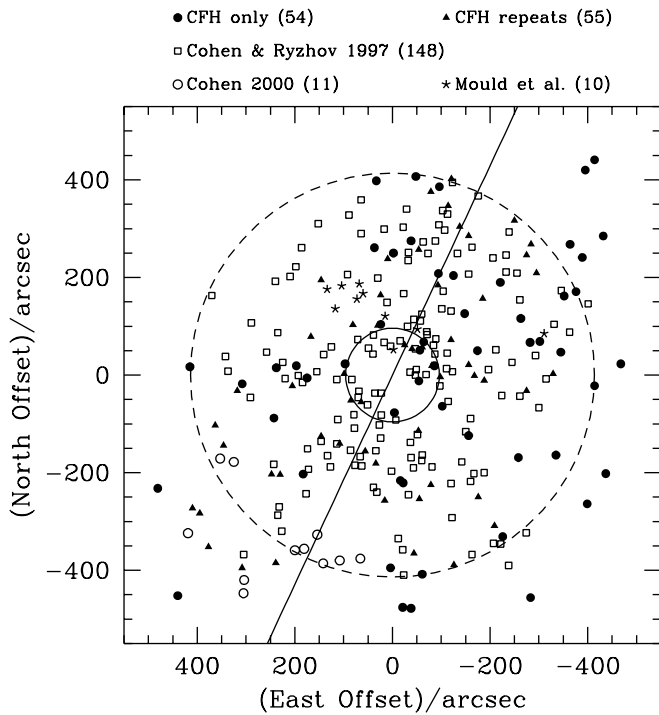


FIG. 2.—Spatial distribution of the 278 confirmed GCs around M87 (i.e., all objects falling within the boxed region of the bottom panel of Fig. 1). The center of the galaxy is at (0, 0), the inner circle marks the effective radius of the stellar mass of M87 ($R_e = 96'' \simeq 7$ kpc), and the outer circle has a radius of $414'' \simeq 30$ kpc $\simeq 4.3R_e$. The diagonal line shows the photometric major axis of the galaxy.

that $\theta = 0$ naturally identifies its rotation axis and its volume density n is a function only of the galactocentric distance r . Also define a projected, circular coordinate system on the plane of the sky by the radial coordinate R and the azimuth Θ . The projected (surface) density of the GCS, N , is, by the spherical hypothesis, a function of R alone:

$$N(R) = 2 \int_R^\infty n(r) \frac{r dr}{\sqrt{r^2 - R^2}}. \quad (3)$$

However, its projected angular velocity, Ω , which is just the average of ω along the line of sight through the GCS, may be a function of R and Θ both. Assuming that the cluster system is viewed so that its rotation axis lies exactly in the plane of the sky and coincides with $\Theta = 0$, we have

$$\Omega(R, \Theta) = \frac{2}{N(R)} \int_R^\infty n(r) \omega(r, \theta) \frac{r dr}{\sqrt{r^2 - R^2}}, \quad (4)$$

where $\cos \theta = (R \cos \Theta)/r$ by simple geometry (see also Fillmore 1986). In addition to this, the angular velocities ω and Ω are related to the linear velocities $\langle v_\phi \rangle$, the intrinsic streaming, or rotation, velocity of the GCS,²⁰ and $\langle v_p \rangle$, the averaged component of velocity along the line of sight, in the usual way: $\omega = \langle v_\phi \rangle / (r \sin \theta)$ and $\Omega = \langle v_p \rangle / (R \sin \Theta)$. Thus,

$$\langle v_p \rangle = 2 \frac{R \sin \Theta}{N(R)} \int_R^\infty n(r) \frac{\langle v_\phi \rangle}{r \sin \theta} \frac{r dr}{\sqrt{r^2 - R^2}}, \quad (5)$$

where $\langle v_\phi \rangle$ may still, in general, be any function of r and θ .

²⁰ The ϕ direction wraps around the rotation axis by definition.

Equation (4) makes it clear that the apparent angular velocity will be a function of R alone, $\Omega = \Omega(R)$, if ω is a function only of r , i.e., if the intrinsic angular velocity of the GCS is constant on spherical surfaces. This is just what is required, as equation (5) shows explicitly, to have $\langle v_p \rangle \propto \sin \Theta$, and thus to justify fitting a sinusoid to our radial velocity data as a function of projected azimuth.

It is worth emphasizing this point, even though it is not new (see, e.g., Fillmore 1986): the projected angular velocity of a spherical GCS is constant on circles in the plane of the sky, so that its linear velocity $\langle v_p \rangle$ varies sinusoidally with projected azimuth Θ , if the intrinsic angular velocity is constant on spheres, such that $\langle v_\phi \rangle \propto \sin \theta$. It happens that the variation of $\langle v_p \rangle$ with Θ in our sample of M87 GCs is adequately described, at all galactocentric radii, by a simple sine curve (see below), and we interpret this as an indication that the angular velocity field of the GCS is stratified approximately on spherical surfaces: $\langle v_\phi \rangle / (r \sin \theta) = \omega(r)$. This interpretation is somewhat different from that adopted by Cohen & Ryzhov (1997) and apparently by Kissler-Patig & Gebhardt (1998), who fit sines to their v_p versus Θ data and then posit that the intrinsic $\langle v_\phi \rangle$ field of the GCS is stratified on cylinders. The only way that both of these assumptions can be simultaneously true, that is, $\langle v_p \rangle \propto \sin \Theta$ and $\langle v_\phi \rangle$ depending on r and θ only through the combination $(r \sin \theta)$, is in the special case of solid-body rotation, $\omega = \Omega = \text{constant}$. This would, of course, require that $\Omega R \propto R$. Unfortunately, the data neither rule out this possibility nor present a compelling case for it (see, e.g., Fig. 8 below). We shall return to the issue of possible solid-body rotation below, and in § 5.7 for the specific case of the metal-poor GCS (see Fig. 19 below).

In summary, we assume that (1) the GCS of M87 can be approximated as spherical [$n = n(r)$ and $N = N(R)$], (2) its angular velocity field is constant on spheres [$\omega = \omega(r)$ and $\Omega = \Omega(R)$], and (3) its rotation axis lies exactly in the plane of the sky and coincides with $\Theta = 0$. We are then able to investigate the rotation of the GCS by fitting our observed radial velocities with the function

$$v_p(\Theta) = v_{\text{sys}} + (\Omega R) \sin(\Theta - \Theta_0), \quad (6)$$

where Θ_0 (measured, as Θ is, in degrees east of north) locates the GCS rotation axis and the rotation amplitude ΩR can in principle be any function of projected galactocentric radius R .

3.2. Global Kinematic Properties

Figure 3 shows the dependence of radial velocity on azimuth for our full sample of 278 GCs in M87, for our subsample of 161 blue clusters (defined by $0.80 \leq C - T_1 \leq 1.42$), and for our subsample of 117 red GCs ($1.42 \leq C - T_1 \leq 2.35$). Overlaid on the data in each case is the best-fit sine. For the full sample, we find a rotation amplitude of $\Omega R = 169_{-97}^{+42}$ km s⁻¹, where the quoted errors refer to 90% confidence intervals. This rotation amplitude is somewhat larger than the value of $\Omega R \sim 100$ km s⁻¹ estimated by Cohen & Ryzhov (1997), although still consistent given the rather large uncertainties. The best-fit position angle of the rotation axis for the full sample is $\Theta_0 = 66^\circ \pm 35^\circ$ east of north. The photometric minor axis of the underlying galaxy light is similarly oriented to $\Theta_{\text{phot}} = 65^\circ$ (Carter & Dixon 1978), a correspondence that is consistent with our simplifying assumption that we are viewing the GCS essentially edge-on. We separately find $\Omega R = 172_{-108}^{+51}$ km s⁻¹ and

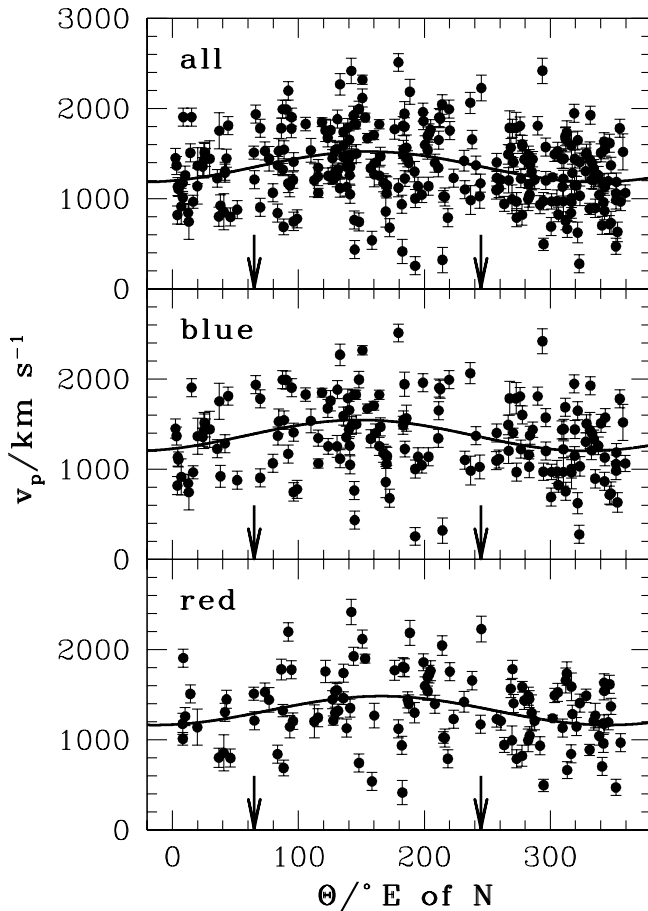


FIG. 3.—Radial velocity vs. azimuth for the full sample of 278 confirmed GCs, and separately for the 161 blue clusters with $0.80 \leq (C - T_1) \leq 1.42$ and the 117 red GCs with $1.42 \leq (C - T_1) \leq 2.35$. The best-fit sine curve, $v_p = v_{\text{sys}} + (\Omega R) \sin(\Theta - \Theta_0)$, is overlaid in each case; see Table 1 for a listing of the parameters. The orientation of the photometric minor axis of M87 is indicated by the vertical arrows in each panel at $\Theta = 65^\circ$ and 245° east of north.

$\Theta_0 = 59^\circ \pm 52^\circ$ for the entire sample of metal-poor clusters and $\Omega R = 160_{-99}^{+120}$ km s $^{-1}$ and $\Theta_0 = 76^\circ \pm 45^\circ$ for the metal-rich sample. The dispersion of velocities about the best-fitting sine is $\sigma_{p,r} = 384_{-32}^{+27}$ km s $^{-1}$ for the full sample, $\sigma_{p,r} = 397_{-49}^{+37}$ km s $^{-1}$ for the metal-poor clusters, and $\sigma_{p,r} = 364_{-52}^{+46}$ km s $^{-1}$ for the metal-rich clusters.

We conclude, therefore, that rotation is present in the M87 GCS and is significant at a high confidence level, for the blue and red subsystems alike. Moreover, the metal-poor and metal-rich clusters in our sample have (1) essentially identical rotation amplitudes, (2) rotation axes that coincide with one another and with the photometric minor axis of the galaxy, and (3) similar fractions of their total kinetic energy stored in rotation [$(\Omega R / \sigma_{p,r})^2 \simeq 0.2 \pm 0.1$ in each case]. Thus, within the observational uncertainties, there is no obvious difference between the global kinematics of the two subsystems. We caution, however, that this is just a thumbnail sketch of the kinematics, averaged over the full range of galactocentric radii spanned by the GCs in our radial velocity sample. As was stressed above, the quantity ΩR can, in principle, be a function of projected radius, as might be the rotation axis Θ_0 and the dispersion of the line-of-sight velocities. While Figure 3 is useful as a rough summary of the situation, it is necessarily limited.

Thus, we sort our GCs into a number of distinct circular annuli and fit sine curves separately to v_p versus Θ in each annulus to investigate possible radial variations in the kinematics of the total, blue, and red cluster systems. Table 1 lists the results of this exercise and includes full details of the global kinematics discussed above. The first column of the table defines the annulus in question (with $1'' = 0.073$ kpc for a distance of 15 Mpc to M87), the second and third columns give the median radius (in arcsec and kpc) of the clusters in that radial bin, and the fourth column records the number of objects in it. The fifth and six columns then give the mean line-of-sight velocity of the clusters (ignoring any rotation that might be present, and estimated using the robust, biweight measure of “location” discussed by Beers, Flynn, & Gebhardt 1990) and the dispersion of their velocities about this mean value (i.e., the biweight “scale” of Beers et al. 1990). The uncertainties on these values, and on all quantities in Table 1, define a 90% confidence interval. They are estimated using a numerical bootstrap procedure in which 1000 artificial data sets are constructed by randomly choosing N clusters from among the actual data in an annulus. The mean and dispersion are computed for each of these 1000 trial data sets, the results are sorted, and the values corresponding to the fifth and 95th percentiles are identified; uncertainties are then defined as the offsets between these values and the actual $\langle v_p \rangle$ and σ_p computed from the real data. The seventh, eighth, and ninth columns of Table 1 give the rotation parameters in each annulus, for each of our GC subsamples. These are determined by an error-weighted, nonlinear, least-squares fit of the sinusoid in equation (6), and their 90% confidence intervals follow from fitting v_p versus Θ for each of the 1000 artificial data sets constructed in the bootstrap procedure just described. Finally, the tenth column of Table 1 gives the (biweight) dispersion of the velocities about the best-fit sine in each annulus for comparison with the previous analyses of Cohen & Ryzhov (1997) and Kissler-Patig & Gebhardt (1998).

Figure 4 directly compares some of the fits from Table 1 against the data. The filled circles in this figure plot v_p against Θ for our blue GCs, while the open circles correspond to the red clusters. The top panel shows the objects with $125'' \leq R < 125''$; the second panel is for those with $125'' \leq R < 207''$; the third panel includes clusters at $207'' \leq R < 297''$; the fourth is for GCs with $297'' \leq R < 380''$; the fifth has $380'' \leq R < 414''$; and the sixth has $414'' \leq R \leq 635''$. In the top four panels, the solid curves trace the corresponding sine fits for the blue clusters, as summarized in Table 1, and the dashed curves are the best-fit sinusoids for the red clusters. In the bottom two panels, the blue and red fits shown are those given in Table 1 for the annuli combined (i.e., for $380'' \leq R \leq 635''$), as these are much more stable and less uncertain. In all cases, the observed $v_p(\Theta)$ data appear to be consistent with the simple sinusoidal form that was assumed in our fitting.

Table 1 and Figure 4 hint at some interesting radial trends in the kinematics of the M87 GCS. First, it appears that the projected kinematics of the red and blue subsystems are, at least to first order, rather similar. There are, however, suggestions of some differences that we shall return to below and in § 5.7, where we discuss the two-dimensional velocity field of the GCS. Second, although it is roughly constant over much of our range in projected radius, the velocity dispersion of the clusters (either about

TABLE 1
KINEMATICS OF THE M87 GLOBULAR CLUSTER SYSTEM

R (arcsec)	$\langle R \rangle$ (arcsec)	$\langle R \rangle$ (kpc)	N	$\langle v_p \rangle$ (km s ⁻¹)	σ_p (km s ⁻¹)	v_{sys} (km s ⁻¹)	Θ_0 (deg east of north)	ΩR (km s ⁻¹)	$\sigma_{p,r}$ (km s ⁻¹)
Full Sample: 278 Clusters with $0.80 \leq (C - T_1) \leq 2.35$									
35–635	252	18.3	278	1335 ⁺⁴³ ₋₄₁	401 ⁺²⁷ ₋₃₀	1354 ⁺⁴² ₋₃₄	66 ⁺³⁶ ₋₃₄	169 ⁺⁴² ₋₉₇	384 ⁺²⁷ ₋₃₂
35–125	91	6.6	55	1392 ⁺⁷⁴ ₋₈₆	318 ⁺³⁷ ₋₆₀	1379 ⁺⁹⁴ ₋₆₈	92 ⁺⁶² ₋₇₀	90 ⁺¹³⁰ ₋₁₄₃	306 ⁺⁴¹ ₋₅₈
125–207	178	12.9	57	1282 ⁺⁹³ ₋₉₀	366 ⁺⁶⁶ ₋₈₂	1312 ⁺⁶³ ₋₁₀₄	-1 ⁺⁵⁶ ₋₄₆	153 ⁺¹³³ ₋₁₄₄	359 ⁺⁵⁸ ₋₈₉
207–297	252	18.3	55	1269 ⁺⁹³ ₋₁₀₄	409 ⁺⁶⁷ ₋₇₉	1248 ⁺¹²⁹ ₋₆₁	127 ⁺⁴³ ₋₅₅	188 ⁺¹³⁸ ₋₁₂₂	388 ⁺⁶⁰ ₋₈₂
297–380	332	24.1	56	1311 ⁺⁸¹ ₋₈₅	332 ⁺⁴⁴ ₋₅₃	1375 ⁺⁶⁶ ₋₁₂₂	49 ⁺⁴⁵ ₋₅₇	199 ⁺¹¹³ ₋₁₁₈	301 ⁺³⁹ ₋₄₉
380–635	415	30.2	55	1445 ⁺¹³⁰ ₋₁₂₉	543 ⁺⁷³ ₋₈₈	1360 ⁺¹⁵⁴ ₋₁₁₉	82 ⁺³⁶ ₋₆₉	303 ⁺¹⁹⁰ ₋₁₅₀	470 ⁺⁹⁶ ₋₉₇
380–414	402	29.2	27	1324 ⁺²⁰⁴ ₋₂₀₃	605 ⁺⁹⁸ ₋₁₃₆	1319 ⁺²³² ₋₁₉₆	45 ⁺⁶⁹ ₋₄₉	361 ⁺⁴³⁶ ₋₂₂₁	514 ⁺¹⁰⁵ ₋₁₇₃
414–635	481	35.0	28	1547 ⁺¹⁷² ₋₁₆₁	460 ⁺⁹³ ₋₁₁₄	1381 ⁺²¹⁴ ₋₉₆	105 ⁺⁴⁵ ₋₅₅	411 ⁺³⁰⁵ ₋₅₉₄	352 ⁺¹⁷⁴ ₋₁₁₈
Metal-Poor Sample: 161 Clusters with $0.80 \leq (C - T_1) \leq 1.42$									
35–635	260	18.9	161	1339 ⁺⁵⁸ ₋₆₃	412 ⁺³⁶ ₋₄₃	1375 ⁺⁴³ ₋₉₂	59 ⁺⁵⁰ ₋₅₃	172 ⁺⁵¹ ₋₁₀₈	397 ⁺³⁷ ₋₄₆
35–125	98	7.1	26	1355 ⁺¹²⁶ ₋₁₁₁	300 ⁺⁵⁸ ₋₈₈	1375 ⁺¹⁰⁹ ₋₉₅	77 ⁺⁷⁶ ₋₇₅	85 ⁺²⁶⁰ ₋₁₆₆	288 ⁺⁴⁷ ₋₁₀₄
125–207	185	13.5	33	1235 ⁺¹¹² ₋₁₁₆	350 ⁺⁹⁶ ₋₁₀₈	1277 ⁺⁹¹ ₋₁₂₅	-37 ⁺⁵⁸ ₋₅₄	162 ⁺²¹⁰ ₋₂₂₉	342 ⁺⁷⁷ ₋₁₁₇
207–297	250	18.2	33	1325 ⁺¹³⁴ ₋₁₄₃	447 ⁺⁸³ ₋₁₀₇	1318 ⁺¹⁸⁰ ₋₉₃	136 ⁺⁴⁵ ₋₅₂	270 ⁺¹⁸¹ ₋₁₈₂	410 ⁺⁸³ ₋₁₂₀
297–380	334	24.3	31	1353 ⁺¹¹⁹ ₋₁₀₆	340 ⁺⁵⁰ ₋₇₁	1445 ⁺³⁶ ₋₁₆₄	37 ⁺³¹ ₋₅₅	253 ⁺¹²⁶ ₋₁₄₁	295 ⁺⁴³ ₋₈₆
380–635	414	30.1	38	1433 ⁺¹⁶⁶ ₋₁₇₂	531 ⁺⁸¹ ₋₁₀₆	1346 ⁺¹⁵⁶ ₋₁₅₂	76 ⁺⁴⁶ ₋₆₄	322 ⁺²²⁹ ₋₂₂₉	452 ⁺⁹⁸ ₋₁₂₈
380–414	404	29.4	19	1291 ⁺²³⁹ ₋₂₅₉	600 ⁺¹²⁶ ₋₂₃₅	1280 ⁺²²⁵ ₋₂₈₂	63 ⁺⁷⁵ ₋₇₇	313 ⁺⁴⁷⁶ ₋₃₃₇	555 ⁺¹¹² ₋₂₄₀
414–635	480	34.9	19	1559 ⁺²⁶³ ₋₁₈₃	412 ⁺⁷¹ ₋₁₇₁	1406 ⁺¹⁹⁹ ₋₁₄₀	94 ⁺²⁹ ₋₄₅	443 ⁺³¹⁶ ₋₂₅₂	303 ⁺⁶¹ ₋₁₅₃
Metal-Rich Sample: 117 Clusters with $1.42 \leq (C - T_1) \leq 2.35$									
35–635	239	17.4	117	1331 ⁺⁶³ ₋₆₆	385 ⁺⁴⁹ ₋₅₁	1324 ⁺⁹³ ₋₇₀	76 ⁺⁴⁴ ₋₄₆	160 ⁺¹²⁰ ₋₉₉	364 ⁺⁴⁹ ₋₅₂
35–125	83	6.0	29	1415 ⁺¹³⁷ ₋₁₂₁	325 ⁺⁷⁰ ₋₉₅	1379 ⁺¹⁵³ ₋₁₁₆	100 ⁺⁷¹ ₋₇₈	93 ⁺¹⁷⁸ ₋₂₅₆	319 ⁺⁶¹ ₋₁₃₇
125–207	172	12.5	24	1341 ⁺¹⁵⁶ ₋₁₃₃	378 ⁺⁹⁵ ₋₁₃₈	1368 ⁺¹¹⁶ ₋₁₅₅	23 ⁺⁵⁵ ₋₆₂	193 ⁺²⁰⁵ ₋₂₄₆	345 ⁺⁸⁸ ₋₁₅₅
207–297	258	18.8	22	1199 ⁺¹³¹ ₋₁₃₇	344 ⁺⁷⁹ ₋₁₁₄	1174 ⁺¹¹⁶ ₋₁₁₆	100 ⁺⁵³ ₋₅₃	183 ⁺¹⁹⁵ ₋₁₁₅	312 ⁺⁴⁴ ₋₁₃₈
297–380	325	23.6	25	1257 ⁺¹⁰⁶ ₋₁₁₉	304 ⁺⁸³ ₋₁₂₀	1271 ⁺¹¹⁶ ₋₁₁₂	104 ⁺⁴³ ₋₅₅	174 ⁺³⁰⁶ ₋₁₉₉	268 ⁺⁵⁵ ₋₁₄₁
380–635	415	30.2	17	1499 ⁺²⁰⁷ ₋₂₇₅	588 ⁺¹¹⁸ ₋₂₇₆	1357 ⁺³²⁴ ₋₂₃₂	90 ⁺⁶⁷ ₋₇₃	289 ⁺⁴⁴¹ ₋₅₉₅	477 ⁺¹⁸⁷ ₋₂₇₀
380–414	399	29.0	8	1433 ⁺⁴⁰⁷ ₋₃₈₇	583 ⁺¹¹⁴ ₋₄₄₂	1350 ^a	18 ⁺⁷³ ₋₅₀	667 ⁺⁴⁸⁷ ₋₁₀₀₀	314 ⁺¹¹² ₋₃₁₄
414–635	481	35.0	9	1512 ⁺²⁸⁴ ₋₂₈₇	568 ⁺¹⁹⁶ ₋₅₆₈	1350 ^a	116 ⁺⁶⁶ ₋₅₈	200 ⁺⁹⁷³ ₋₁₀₅₀	432 ⁺³⁶⁰ ₋₄₃₂

^a Systemic velocity held fixed in fit of sine curve.

the sample mean $\langle v_p \rangle$ or about the best-fit sine curve) shows some evidence for an increase at the largest R . This is just significant at the 90% level in our sample (and not even then for the metal-rich subsystem), but it is actually predicted by the simple dynamical models we present in § 4. Third, there is some evidence for a rise in the rotation amplitude ΩR at large radii, although this is not formally significant at the 90% level; to this degree of accuracy, the red and blue cluster samples are both consistent with a constant $\Omega R \sim 170 \text{ km s}^{-1}$ at all radii $2.5 \lesssim R \lesssim 35 \text{ kpc}$ (see Fig. 8 below). On the other hand, the angle of the rotation axis, Θ_0 , does change significantly as a function of radius, particularly among the blue clusters. This interesting phenomenon is discussed in more detail below.

3.3. Kinematic Properties as a Function of Projected Radius

In order to visualize these trends better and to address any concerns that our particular choice of bins in Table 1 might have influenced our results, Figures 5–8 show the line-of-sight mean velocity and dispersion, as well as the best-fit rotation axis and amplitude, as functions of projected radius for our full GC sample and separately for each of the blue and red subsets. To construct these profiles, we slide a bin of fixed radial width $\Delta R = 90'' \simeq 6.5 \text{ kpc}$ through the GCS, centering the bin at the position of each of our measured GCs in turn and computing the kinematics (including bootstrap estimates of confidence intervals) for all clusters lying within $\pm(\Delta R)/2$ of that point. We begin at small projected radii when the number of clusters per bin

first exceeds 15 (so that the fits can be usefully constrained), and we stop at large R when the sample size per bin drops below this limit.

Clearly, most of the points plotted in these figures are not statistically independent (only points separated by at least the full $\Delta R = 6.5 \text{ kpc}$, the size of the horizontal bar drawn in each middle panel, can be), and we do not attempt any sort of formal fits to these profiles. Nevertheless, this procedure is useful since it provides a more detailed (albeit smoothed) view of radial trends than can be had with a single binning such as that in Table 1. It is also important to note that this method of smoothing the data is different than that employed by Kissler-Patig & Gebhardt (1998) and Cohen (2000). These authors opt instead to fit the kinematics in a series of annuli that always enclose the same number of data points and therefore (because neither the intrinsic spatial distribution of the GCS nor the observational sampling of it is uniform) have a variable radial width (for an illustration of this point see Fig. 2 of Cohen 2000). Our approach avoids the nontrivial difficulty of interpreting data that have been smoothed by different amounts from point to point, and it yields a more accurate, though necessarily less precise, depiction of radial variations in kinematics at the low-density, large-radius limits of our GC sample.

The mean velocity in Figure 5, which makes no allowance or corrections for rotation, shows no significant variations with radius until roughly $R \gtrsim 30 \text{ kpc}$. The sharp apparent rise in $\langle v_p \rangle$ at this radius is due (as Fig. 2 and the bottom of

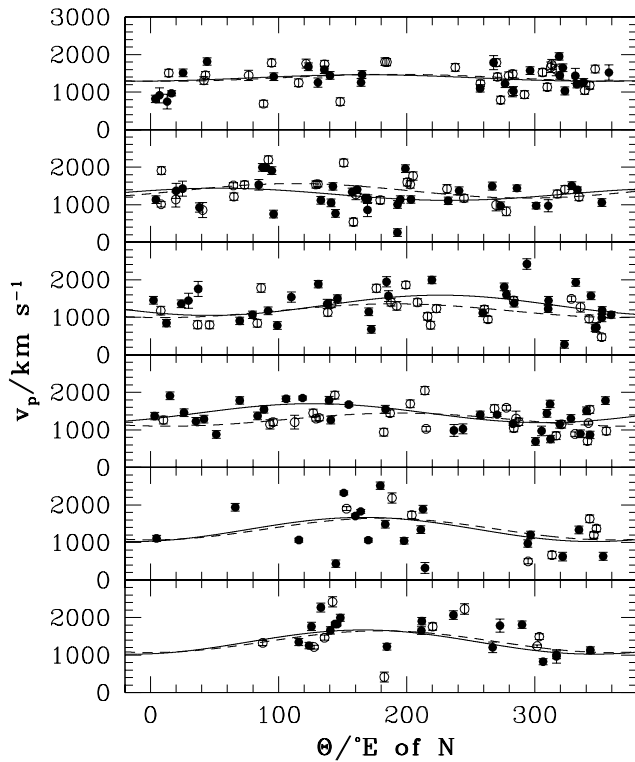


FIG. 4.—Line-of-sight velocity vs. azimuth for M87 GCs in six radial bins. From top to bottom, the panels show clusters in the following ranges: (1) $35'' \leq R < 125''$; (2) $125'' \leq R < 207''$; (3) $207'' \leq R < 297''$; (4) $297'' \leq R < 380''$; (5) $380'' \leq R < 414''$; (6) $414'' \leq R \leq 635''$. Filled circles are metal-poor (blue) GCs, and solid lines are their best-fit sine curves with parameters given in Table 1. Open circles denote the metal-rich (red) GCs, and dashed lines trace the best-fit sine curves (with parameters also given in Table 1). Note that the identical sine curves shown in the bottom two panels have been derived from the combined data, i.e., using all clusters in the range $380'' \leq R \leq 635''$.

Fig. 4 both show, and as Romanowsky & Kochanek 2001 also suggested) to sparse sampling of a population that shows significant rotation: the few GCs in our radial velocity sample at these large radii have been drawn mostly from positions around the photometric major axis of M87 (at 155° east of north), where the rotation produces line-of-sight velocities farthest from the true systemic velocity of the galaxy and the GCS. Fitting a sine curve to quantify the rotation at every radius takes this effect into account, and a plot of v_{sys} versus R (see eq. [6]) is essentially flat and consistent with a constant $v_{\text{sys}} \equiv 1350 \text{ km s}^{-1}$.

The velocity dispersion profiles in Figure 6 show both the biweight rms scatter, σ_p , about the direct mean of the sample in each bin (*filled circles*) and the biweight dispersion, $\sigma_{p,r}$, about the best-fitting sine curve (*open circles*). At relatively small projected radii $R \sim 10\text{--}15$ kpc, the red clusters may be dynamically somewhat “hotter” than the blue clusters in M87, and the situation may be reversed at larger radii. As was mentioned above, however, in connection with Table 1, these apparent differences are not statistically significant. However, in agreement with previous studies (e.g., Cohen & Ryzhov 1997), we do see evidence for a rising velocity dispersion toward larger radii, a trend that is more clearly established for our blue clusters than for the red ones.

Figures 7 and 8, which show the rotation axis position angle and apparent rotation amplitude as functions of pro-

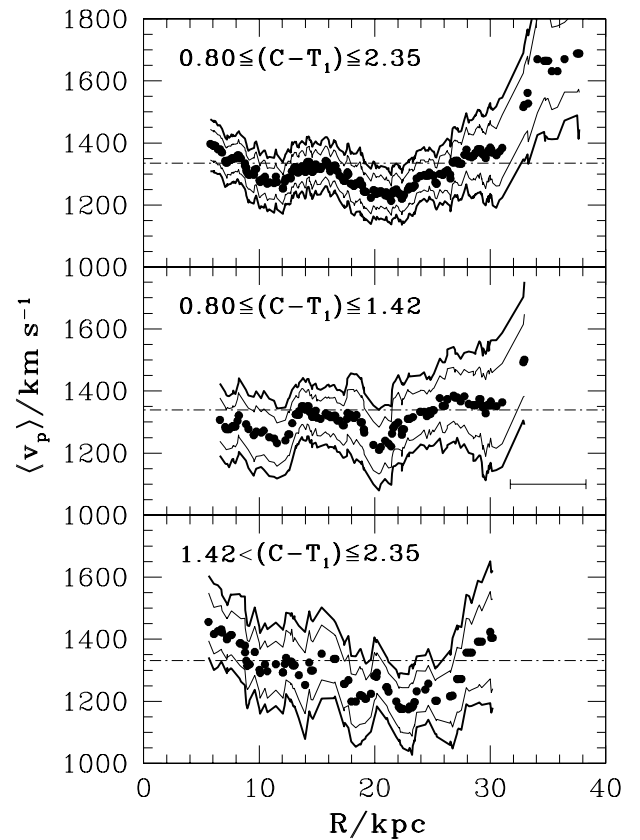


FIG. 5.—Upper Panel: Biweight estimates for the mean line-of-sight velocity of the M87 GCS, as a function of distance from galaxy center (*filled circles*). Thin and thick solid lines show the 68% and 90% confidence limits on $\langle v \rangle$, estimated using a bootstrap technique as described in the text. Circles represent the systemic velocity measured in radial bins of constant width $\Delta R \equiv 90'' \simeq 6.5$ kpc (indicated by the error bar in the middle panel). The dashed horizontal line indicates the mean velocity recorded in Table 1 for clusters at all radii $35'' \leq R \leq 635''$. Middle Panel: Same as above, but for the sample of metal-poor (blue) clusters. Lower Panel: As above, but for the sample of metal-rich (red) clusters.

jected radius in the M87 GCS, present the most substantial new result of this empirical part of our analysis and constitute a point of clear departure from earlier studies. These profiles were obtained by fitting equation (6) to the $v_p(\Theta)$ data in our sliding radial bin, with $v_{\text{sys}} \equiv 1350 \text{ km s}^{-1}$ held fixed but with Θ_0 and ΩR both allowed to vary. The most striking point relates to the blue clusters, which appear (see Fig. 7) to rotate about the projected major axis of M87 ($\Theta_0 = -25^\circ$ east of north) in the inner regions of the system, $R \lesssim 16\text{--}18$ kpc, but then switch to the more conventional minor-axis rotation ($\Theta_0 = 65^\circ$ east of north) that they show for $R \gtrsim 20$ kpc. Given the smoothing kernel that we have applied to the data (again, $\Delta R = 90'' \simeq 6.5$ kpc, as illustrated in the middle panel of Fig. 7), this 90° flip in Θ_0 seems to be almost instantaneous. It is probably no accident that it appears to coincide with the onset, at $R \simeq 19$ kpc, of the cD envelope in the starlight (de Vaucouleurs & Nieto 1978; Carter & Dixon 1978) and the GCS of M87 (McLaughlin, Harris, & Hanes 1993). Figures 7 and 8 also reveal that the rotation axis of the red clusters seems to show a gradual drift toward the photometric major axis of M87 for $R \lesssim 18$ kpc before it “corrects” to a constant $\Theta_0 \simeq 65^\circ$ at larger radii. It is not clear, however, that this apparent difference in the small- R behavior of the red and

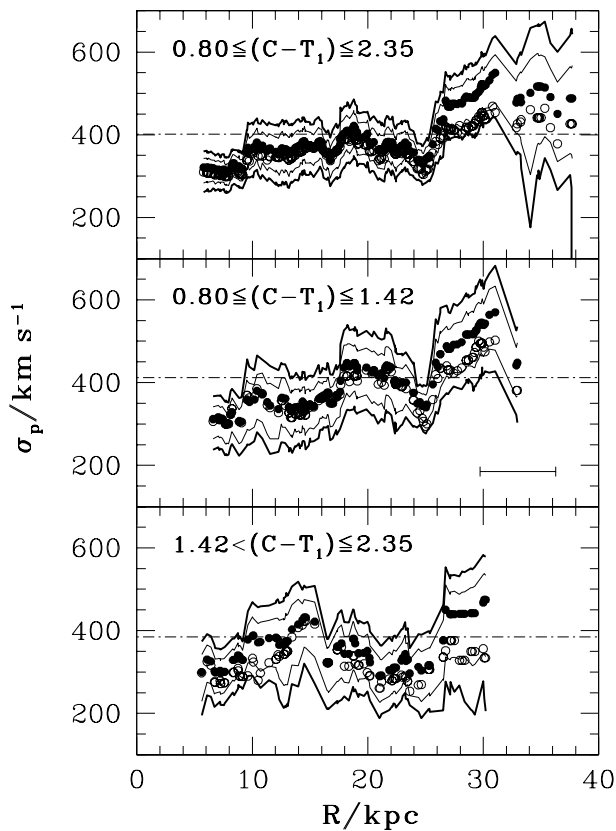


FIG. 6.—*Upper Panel*: Biweight estimates for the velocity dispersion of the M87 GCS as a function of galactocentric distance. Filled circles denote the dispersion σ_p about the sample mean in each bin, taken from Fig. 5. Open circles represent the dispersion $\sigma_{p,r}$ about the best-fitting sine curve in each case (parameters taken from Figs. 7 and 8). Solid curves delimit the 68% and 90% confidence bands for σ_p , obtained from a numerical bootstrap. Horizontal line is at the value determined for the full sample of clusters with $35'' \leq R \leq 635''$. *Middle Panel*: As above, but for the sample of metal-poor (blue) GCs. *Lower Panel*: As above, for the sample of metal-rich (red) clusters.

blue GCs is statistically significant, even at the 68% confidence level. We return to this issue in § 5, where the two-dimensional rotation fields of the metal-poor and metal-rich GC samples are discussed within the context of the larger Virgo Cluster environment.

Figure 8 shows the rotation amplitude corresponding to each fitted value of Θ_0 in Figure 7. As was suggested above, it is difficult to discriminate between a flat rotation curve and one that rises with increasing radius. For instance, there is some evidence for an outward rise in ΩR for $R \gtrsim 25$ kpc, for the red and blue GCs alike, but this effect sets in roughly where the azimuthal coverage of our radial velocity sample begins to decline (see Figs. 2 and 4), and it is significant at just the 68% confidence level. In addition, note that the dashed curve drawn in all three panels of Figure 8 shows the circular velocity of the M87/Virgo potential in which the GCs are orbiting ($v_c(r) = [GM(r)/r]^{1/2}$; see eq. [11] below for our adopted mass model). The fact that ΩR appears to approach this limit at our largest sampled radii suggests that the sparser spatial coverage there may be biasing our results to some extent; it may also provide some evidence that the M87 GCS is being viewed nearly edge-on, as any inclination correction is likely to be small if the apparent ΩR is already so near $v_c(r)$.

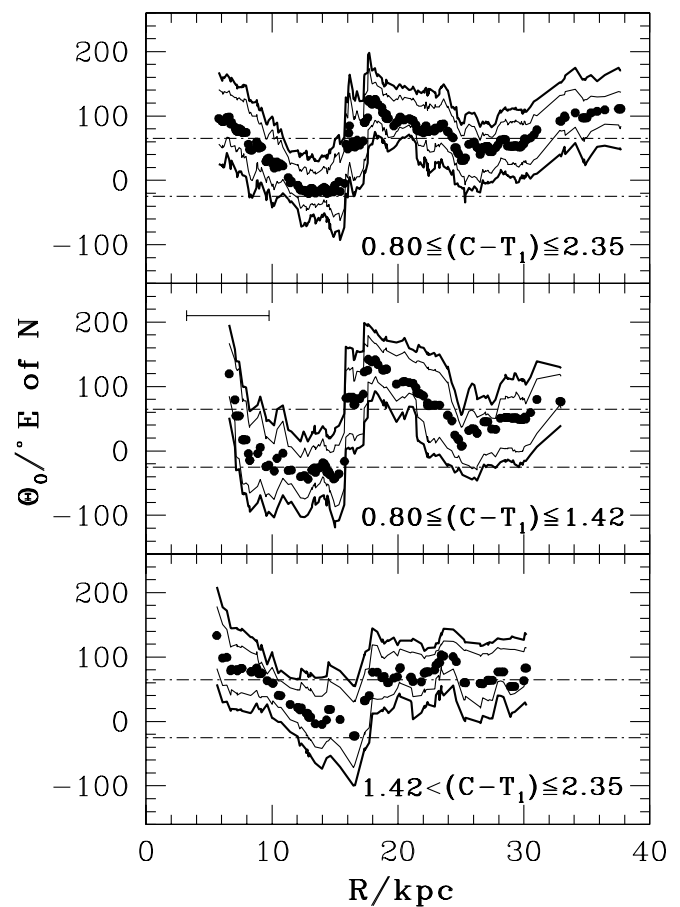


FIG. 7.—*Upper Panel*: Projected azimuth of the rotation axis of the full M87 GCS, as a function of projected galactocentric radius (*filled circles*). Thin and thick solid lines define 68% and 90% confidence bands. In this figure and the following one, the systemic velocity was held fixed at $v_{\text{sys}} = 1350 \text{ km s}^{-1}$ (see Table 1). The upper and lower horizontal lines indicate position angles of the projected major ($\Theta_0 = -25^\circ$) and minor ($\Theta_0 = 65^\circ$) axes of M87. *Middle Panel*: For the metal-poor (blue) GCs. *Lower Panel*: For the metal-rich (red) GCs.

One other point worthy of note in these ΩR profiles is the apparent dip to nearly 0 at radii $R \sim 14\text{--}18$ kpc. This may simply be an artifact of smoothing the data rather than an indication of any real feature in the intrinsic velocity field of the GCS. Since Θ_0 appears to change very suddenly by roughly 90° at some radius in this range, it is conceivable that the 6.5 kpc wide annular bins centered on points in this part of the GCS are simply combining two distinct samples of clusters, rotating about essentially orthogonal axes, whose sinusoidal $v_p(\Theta)$ dependences interfere destructively and average out to a lower amplitude of apparent rotation.

Using the spectroscopic metallicities of Cohen et al. (1998), Kissler-Patig & Gebhardt (1998) attempted to distinguish between metal-poor and metal-rich clusters in their study of the rotation properties of the M87 GCS. They concluded that the blue clusters showed essentially no rotation, $\Omega R \simeq 0$, for small radii $R \lesssim 15$ kpc. However, they fixed Θ_0 at about 30° east of north in their analysis and solved only for the amplitude when fitting sines to their $v_p(\Theta)$ data. The difference between their result and ours for the blue-GCS rotation amplitude stems from the fact that we have found Θ_0 at small R to be far away (i.e., approaching 90°) from the position angle adopted by Kissler-Patig & Gebhardt (1998).

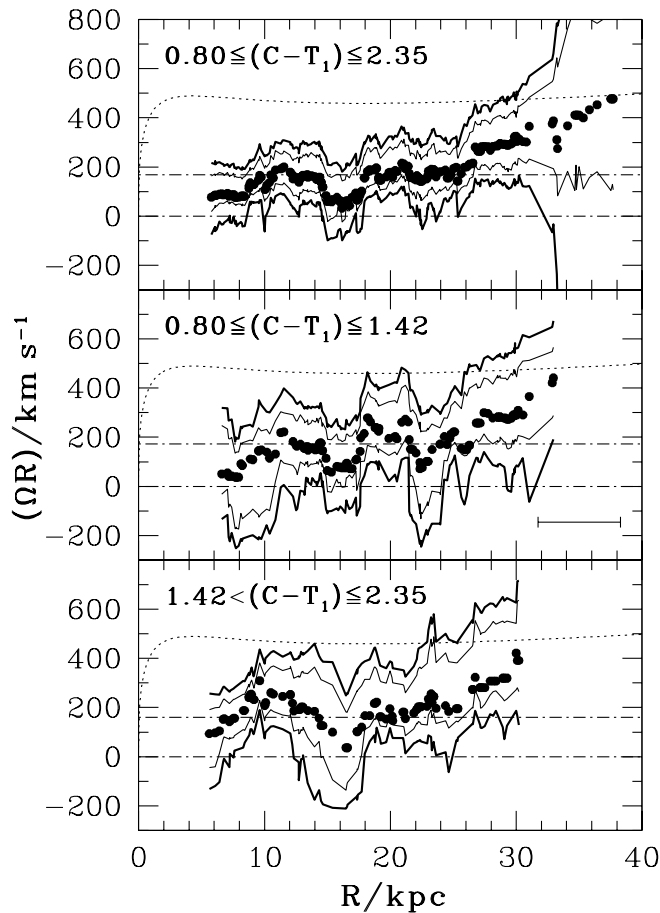


FIG. 8.—*Upper Panel*: Amplitude of projected rotation as a function of galactocentric radius in the M87 GCS (*filled circles*), shown with 68% and 90% confidence bands (*thin and thick solid lines*). The position angle, Θ_0 , of the rotation axis was allowed to vary with radius in the sinusoidal fits (see Fig. 7), but the systemic velocity was held fixed at $v_{\text{sys}} \equiv 1350 \text{ km s}^{-1}$ (see Table 1). Upper horizontal dot-dashed line is placed at the amplitude $\Omega R = 169 \text{ km s}^{-1}$ found by fitting to the entire sample of GCs, over all radii (see Table 1). Dotted curve shows the circular velocity as a function of radius in the M87/Virgo gravitational potential, $v_c(r) = [GM(r)/r]^{1/2}$. *Middle Panel*: As above, but for the sample of metal-poor (blue) clusters. *Lower Panel*: As above, but for the sample of metal-rich (red) clusters.

The acquisition of still more radial velocities for M87 GCs will be important in confirming our findings and in clarifying and quantifying any dichotomies that might exist in the blue versus red kinematics. Meanwhile, the surprisingly complicated rotation field that we have uncovered demands the development of sophisticated dynamical models of the GCS. In particular, although we proceed in the next section with a standard, one-dimensional Jeans equation analysis of velocity moments in the M87 GCS, we recognize that we cannot hope thereby to account rigorously for the dynamical effects of rotation. In fact, in this analysis we shall neglect rotation altogether, treating it as a perturbation to be addressed in future studies.

Figure 9 roughly quantifies the effect this choice may have on our results by comparing the rotation amplitude of the M87 GCS to its line-of-sight velocity dispersion, both about the sample mean (*filled circles*) and about the best-fit sine (*open circles*), at every projected radius. The ratio of the two is essentially constant with projected radius, holding at a level of about 0.45 for the GCS as a whole and for the metal-poor and metal-rich subsamples individually. Thus,

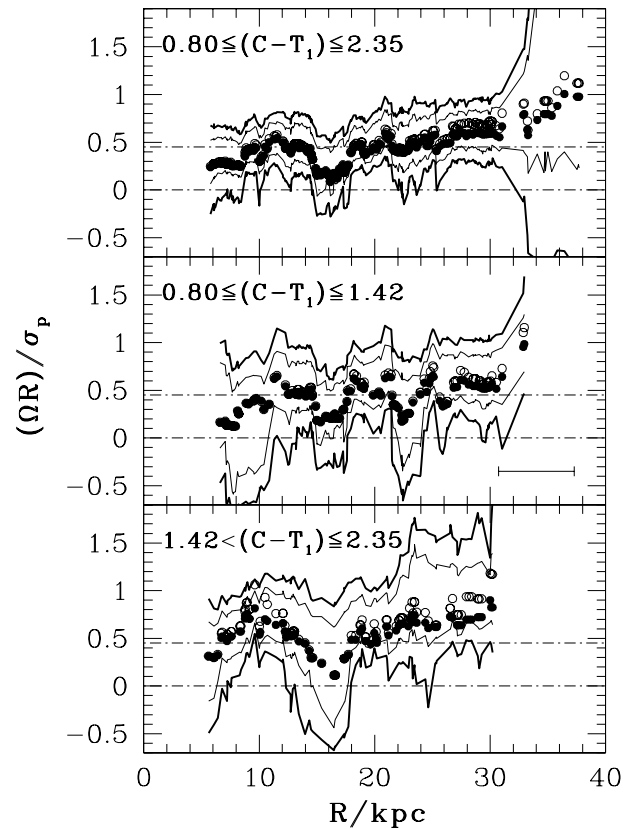


FIG. 9.—*Upper Panel*: Ratio of the projected rotation amplitude in Fig. 8 to the line-of-sight velocity dispersion in Fig. 6. Filled circles compare ΩR to the biweight dispersion σ_p about the mean velocity $\langle v_p \rangle$ at each radius, and the solid lines trace the 68% and 90% confidence limits on the ratio. Open circles come from comparing ΩR to the biweight dispersion $\sigma_{p,r}$ about the best-fitting sine curve at each radius. For clarity, the confidence bands for this second ratio are not shown. The upper horizontal line marks the average of $\langle (\Omega R)/\sigma_p \rangle = 0.45$ suggested by a fit to all clusters in our sample, regardless of radius (see Table 1). *Middle Panel*: As above, but for the metal-poor (blue) GCs. *Lower Panel*: As above, for the metal-rich (red) GCs.

rotation enters as a correction at the $(\Omega R/\sigma_p)^2 \sim 20\%$ level in the Jeans equation analysis that we shall pursue below and at this exploratory stage, is a relatively small source of uncertainty.

4. DYNAMICAL MODELS

In the absence of rotation and the approximation of spherical symmetry, the fundamental equation of our dynamical analysis is the spherical Jeans equation (e.g., Binney & Tremaine 1987):

$$\frac{d}{dr} n_{\text{cl}} \sigma_r^2 + \frac{2\beta_{\text{cl}}}{r} n_{\text{cl}} \sigma_r^2 = -n_{\text{cl}} \frac{GM_{\text{tot}}(r)}{r^2}, \quad (7)$$

where $n_{\text{cl}}(r)$ is the volume density profile of the GCS, $\sigma_r(r)$ is its velocity dispersion in the radial direction, and $\beta_{\text{cl}}(r) \equiv 1 - \sigma_\theta^2/\sigma_r^2$ is a measure of its velocity anisotropy.²¹

The tendency in previous studies along these lines has been to use the projected velocity dispersions of the GCs to

²¹ Considerations of symmetry imply that the two tangential velocity dispersions are equal, i.e., $\sigma_\theta = \sigma_\phi$.

infer the intrinsic $\sigma_r(r)$ and thus to constrain the total, “background” gravitating mass profile $M_{\text{tot}}(r)$. To do so, however, requires some a priori assumptions on the anisotropy profile, $\beta_{\text{cl}}(r)$, and typically this has meant adopting the simplest case of isotropic orbits with $\beta_{\text{cl}} \equiv 0$ (see, e.g., Cohen & Ryzhov 1997). By contrast, Romanowsky & Kochanek (2001) apply a technique in which an ad hoc functional form of $M_{\text{tot}}(r)$ is assumed a priori, and the observed $\sigma_p(R)$ is used in conjunction with sophisticated orbit modeling to constrain both the normalization of the M87/Virgo mass profile and the behavior of $\beta_{\text{cl}}(r)$ in the GCS. The latter procedure is closer in spirit to ours here, in which we specify both $n_{\text{cl}}(r)$ and $M_{\text{tot}}(r)$ in full and then use the observed $\sigma_p(R)$ profiles of § 3 to infer something about the anisotropy of the GC orbits in M87, both globally (for our entire sample) and separately (for the metal-poor and metal-rich populations).

One way to do this is as an “inverse problem” (e.g., Merritt & Oh 1997). In this approach, the observed function $\sigma_p(R)$ is approximated in some model-independent way (e.g., via splines). For an assumed $M_{\text{tot}}(r)$, the two unknown functions $\sigma_r(r)$ and $\beta(r)$ then follow uniquely from the Jeans equation and the deprojection integral. But given the limited number of velocities in our sample, to say nothing of our neglect of rotation and our assumption of spherical symmetry, we opt instead to construct a suite of model $\sigma_p(R)$ profiles by specifying $\beta_{\text{cl}}(r)$ a priori and then comparing these models with the data to gain a broad, qualitative view of the orbital properties of the M87 GCS. Formally, we solve equation (7) for $\sigma_r(r)$:

$$\sigma_r^2(r) = \frac{1}{n_{\text{cl}}(r)} \exp\left(-\int \frac{2\beta_{\text{cl}}}{r} dr\right) \times \left[\int_r^\infty n_{\text{cl}} \frac{GM_{\text{tot}}}{x^2} \exp\left(\int \frac{2\beta_{\text{cl}}}{x} dx\right) dx \right]. \quad (8)$$

With $\sigma_r(r)$ in hand, the projected velocity dispersion profile, $\sigma_p(R)$, then follows from the standard integral

$$\sigma_p^2(R) = \frac{2}{N_{\text{cl}}(R)} \int_R^\infty n_{\text{cl}} \sigma_r^2(r) \left(1 - \beta_{\text{cl}} \frac{R^2}{r^2}\right) \frac{r dr}{\sqrt{r^2 - R^2}}, \quad (9)$$

where the projected GCS density $N_{\text{cl}}(R)$ is given by equation (3). We also compute the cumulative, aperture velocity dispersion profile, defined to be the rms line-of-sight velocity for all clusters inside a given radius:

$$\sigma_{\text{ap}}^2(\leq R) = \left[\int_0^R N_{\text{cl}}(R) \sigma_p^2(R) R dR \right] \times \left[\int_0^R N_{\text{cl}}(R) R dR \right]^{-1}. \quad (10)$$

This statistic has the obvious advantage of reduced noise in the measured dispersion at large radii, although its interpretation can be somewhat more complicated since it reflects a coarse average (and progressively more so as R increases) of a spatially varying quantity.

To proceed in this way, we require accurate descriptions of (1) the total gravitating mass profile in M87 (and, as the projection integrals above make clear, in the Virgo Cluster beyond our last observed galactocentric radius) and (2) the spatial distribution of the full M87 GCS and of the blue and red clusters, $n_{\text{cl}}(r)$, individually.

First, we take $M_{\text{tot}}(r)$ directly from McLaughlin (1999a), who has developed a simple mass model for M87 and Virgo that satisfies all observational constraints imposed by the optical surface photometry of the galaxy (as a tracer of the stellar mass density; de Vaucouleurs & Nieto 1978), by the X-ray surface brightness on $R \lesssim 200$ kpc scales in the core of the cluster (used under the assumption that the hot intra-cluster gas around M87 is in hydrostatic equilibrium with the total mass distribution; Nulsen & Böhringer 1995), and by the spatial distribution and line-of-sight velocity dispersion of the early-type (mostly dE) Virgo galaxies out to scales of ~ 3 Mpc (Binggeli et al. 1985; Girardi et al. 1996). We emphasize that because this model for $M_{\text{tot}}(r)$ was constructed explicitly without any reference to GCS data, it is completely separate from, and independent of, our radial velocity observations. Thus, the total (baryonic and dark) mass interior to any three-dimensional radius r in Virgo is taken to be, with normalizations appropriate for a distance of 15 Mpc to the cluster,

$$\begin{aligned} M_{\text{tot}}(r) &= M_{\text{stars}}(r) + M_{\text{dark}}(r), \\ M_{\text{stars}}(r) &= 8.10 \times 10^{11} M_\odot \left(\frac{r/5.1 \text{ kpc}}{1 + r/5.1 \text{ kpc}} \right)^{1.67}, \\ M_{\text{dark}}(r) &= 7.06 \times 10^{14} M_\odot \\ &\times \left[\ln \left(1 + \frac{r}{560 \text{ kpc}} \right) - \frac{r/560 \text{ kpc}}{1 + r/560 \text{ kpc}} \right]. \quad (11) \end{aligned}$$

Note that this model attributes all of the dark matter around M87 to the Virgo Cluster as a whole; all of the available data are consistent with this minimalist hypothesis, in which M87 as a galaxy has no dark matter halo of its own (see McLaughlin 1999a). The functional form of $M_{\text{dark}}(r)$ is that expected for the “universal” dark matter halo of Navarro, Frenk, & White (1997), in which the volume density scales as $\rho_{\text{dark}} \sim r^{-1}(r_s + r)^{-2}$, with a fitted value of $r_s = 560$ kpc. The adopted models for $M_{\text{stars}}(r)$, $M_{\text{dark}}(r)$, and $M_{\text{tot}}(r)$ are illustrated in Figure 10.

Next, Figure 11 motivates our favored model for the density profile of the full M87 GCS. This plot, which is taken nearly in full from McLaughlin (1999b) and which is described in detail there, shows the volume mass densities of the stars in M87 (obtained by applying a spatially constant mass-to-light ratio to the optical surface photometry of M87), the GCs around the galaxy (obtained by combining number counts from a number of different studies and applying a geometrical deprojection algorithm), and the hot, X-ray-emitting gas in the core of Virgo (obtained in a model-independent way from *ROSAT* observations by Nulsen & Böhringer 1995). The dot-dashed line running through the gas data points is directly proportional to the density profile of the dark matter halo just discussed, i.e., it shows that $\rho_{\text{gas}} \propto \rho_{\text{dark}} \propto (r/560 \text{ kpc})^{-1}(1 + r/560 \text{ kpc})^{-2}$ in Virgo (see McLaughlin 1999a).

The GC density data in Figure 11 have been scaled up by a factor of $1/0.0026 \sim 385$ to illustrate that, beyond a radius of $r \approx 7$ kpc (the effective radius of the M87 starlight in projection), a strict proportionality ties the density of the GCS to that of the other baryons: $\rho_{\text{cl}}(r) = 0.0026[\rho_{\text{stars}}(r) + \rho_{\text{gas}}(r)]$. The constant of this proportionality, 0.0026, appears to hold similarly in nearly 100 other early-type galaxies, and it has been interpreted by McLaughlin (1999b)

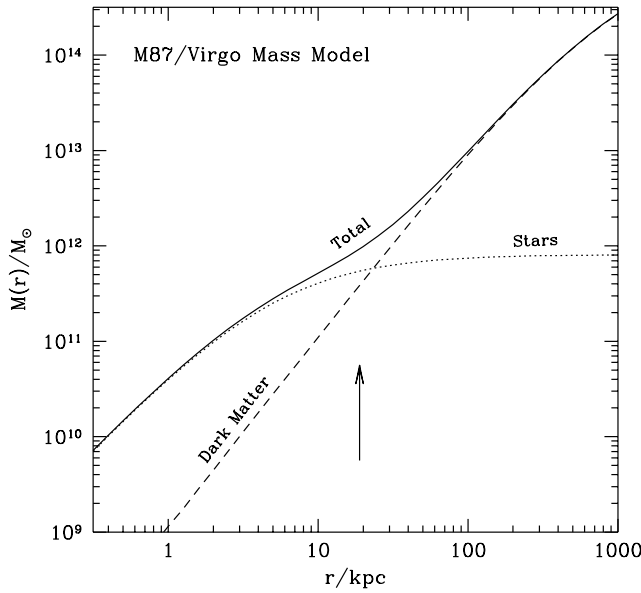


FIG. 10.—Mass model for the central regions of the Virgo Cluster, adopted from McLaughlin (1999a). The solid curve shows the total mass profile, i.e., the combined Virgo Cluster dark matter distribution (as traced by the X-ray-emitting gas) and that of the stellar component of M87, indicated by the dashed and dotted curves, respectively. See § 4 and eq. (11) for details. The vertical arrow shows the projected radius where the cD envelope of M87 begins.

as a universal efficiency of GC formation. Thus, for radii $r \gtrsim 100$ kpc, where there are no direct observations of the GCS density profile, we assume that $\rho_{cl}(r) \simeq 0.0026 \rho_{gas}(r) \propto \rho_{dark}(r)$. Inside this, we adopt an ad hoc functional fit to the GCS density data from McLaughlin (1999b). In total, we

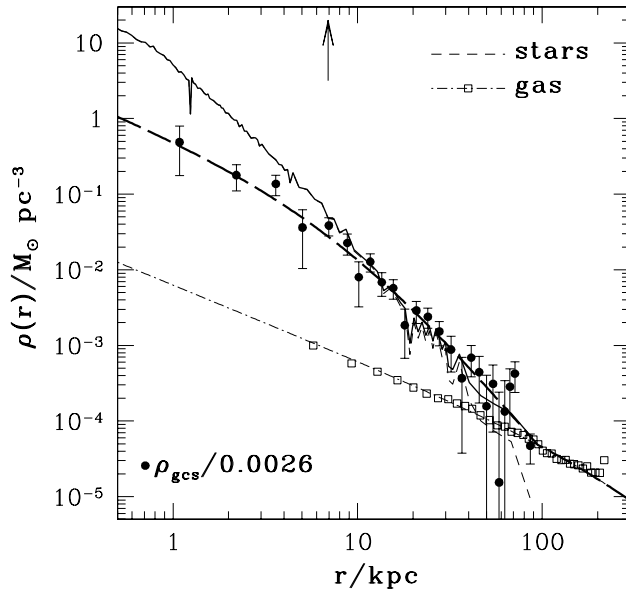


FIG. 11.—Comparison of the (mass) volume density profiles of the GCS (filled circles and thick dashed line), halo stars (thin dashed line), and X-ray gas (open squares and dot-dashed line) around M87 (after McLaughlin 1999b). Note that ρ_{cl} has been scaled upward by the factor $1/0.0026$ (see text). The solid line is the sum of the stellar and gas densities, which have been calculated by deprojecting the galaxy surface photometry with the algorithm of McLaughlin (1999b). The vertical arrow marks the projected effective radius of the galaxy light, $R_{eff} = 96'' \simeq 7$ kpc (de Vaucouleurs & Nieto 1978). Beyond this, it is found that $\rho_{cl} \propto (\rho_{stars} + \rho_{gas})$.

posit that

$$n_{tot}(r) \propto \begin{cases} \left(\frac{r}{9.1 \text{ kpc}}\right)^{-1} \left(1 + \frac{r}{9.1 \text{ kpc}}\right)^{-2}, & r < 95 \text{ kpc}, \\ \left(\frac{r}{560 \text{ kpc}}\right)^{-1} \left(1 + \frac{r}{560 \text{ kpc}}\right)^{-2}, & r > 95 \text{ kpc}. \end{cases} \quad (12)$$

The normalization of this model, which is drawn as the thick, dashed line in Figure 11, is unimportant for our purposes (see eq. [8]). The observed proportionality between the GC and gas density profiles has some important implications for the debate over whether some or all of the GCs surrounding M87 are intergalactic in nature (White 1987; West et al. 1995; Harris et al. 1998). We shall return to this issue in § 5.7.

Figure 12 shows the projection of this density model as a thick solid line. (The mass surface density Σ is related to ρ in the same way as the projected number density N is related to n .) The small triangles are the observed surface densities, again taken from McLaughlin (1999b), that were deprojected to provide the volume densities in Figure 11. We have now also used our new CT_1 photometry to measure the surface density profiles, not only for the complete GC sample but also for the metal-poor and metal-rich samples separately. To do so, our initial catalog of point sources was first trimmed to exclude all objects having $T_1 \geq 22$, $C - T_1 \leq 0.8$, and $C - T_1 \geq 2.35$, leaving us with a sample of 2130 candidate GCs. The adopted limiting magnitude was chosen to ensure that our photometric catalog is complete over the full range in galactocentric radius (see D. Geisler et al. 2001, in preparation). A background surface density of 0.8 clusters arcmin^{-2} was then subtracted to give the surface density profile for the entire cluster population. This background level was chosen based on a comparison of our

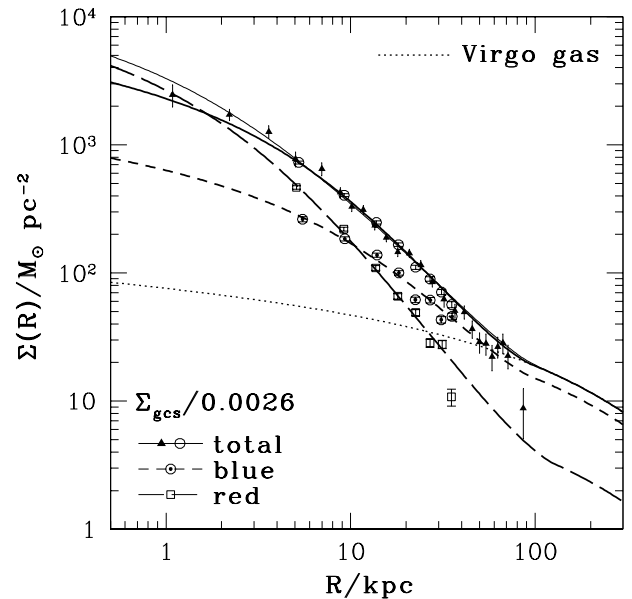


FIG. 12.—Surface density profiles, $\Sigma(R)$, for GCs associated with M87. Triangles show the surface density profile of McLaughlin (1999b) for the full GCS, while open circles show the profile found here using the Washington photometry described in Paper I. Circled points and open squares indicate the respective surface density profiles of metal-poor (blue) and metal-rich (red) GCs. The thick curves correspond to projections of the models in eqs. (12)–(14) in the text; see the discussion there for details.

surface density profile with the calibrated surface density profile of McLaughlin (1999b) and agrees to $\simeq 5\%$ with that predicted by the Galactic star count model of Bahcall & Soneira (1981). The final, blue-plus-red profile is shown as the open circles in Figure 12, where it has been scaled vertically to match the counts from McLaughlin (1999b) and shows good agreement with that independent measurement of $\Sigma_{\text{cl}}(R)$.

For the separate metal-rich and metal-poor samples, we have taken the background surface densities to be exactly half that of the total background in our CT_1 sample. Though somewhat arbitrary, these choices of backgrounds are consistent with the color distribution of foreground stars predicted by Ratnatunga & Bahcall (1985) for three Galactic GCs having Galactic latitudes and longitudes similar to M87. This approach is obviously inferior to measuring surface densities directly from background fields, but the precise choice of backgrounds has relatively little effect on the final surface density profiles, except in the outermost bins. The resulting distributions for the metal-rich and metal-poor cluster populations are indicated by the open squares and circled points in Figure 12. This shows quite clearly that the metal-poor clusters in M87 follow a much shallower radial profile than their metal-rich counterparts, consistent with earlier findings based on *Hubble Space Telescope* (*HST*) imaging in the central regions of the galaxy (e.g., Neilsen, Tsvetanov, & Ford 1999). There is no reasonable choice of background that can alter this basic conclusion. Even if we were to make the highly implausible assumption that the background consists entirely of sources having colors of $C - T_1 \leq 1.42$, this qualitative contrast between the blue and red GCSs would remain.

A more detailed discussion of the spatial distribution of the M87 GCS will be presented in D. Geisler et al. (2001, in preparation); our purposes only require estimations of the overall shapes of $n_{\text{blue}}(r)$ and $n_{\text{red}}(r)$. To obtain these, we project models similar in form to that in equation (12) and fit to the blue- and red-GCS data points in Figure 12. We obtain

$$n_{\text{blue}}(r) \propto \begin{cases} \left(\frac{r}{20.5 \text{ kpc}}\right)^{-1} \left(1 + \frac{r}{20.5 \text{ kpc}}\right)^{-2}, & r < 95 \text{ kpc}, \\ \left(\frac{r}{560 \text{ kpc}}\right)^{-1} \left(1 + \frac{r}{560 \text{ kpc}}\right)^{-2}, & r > 95 \text{ kpc}, \end{cases} \quad (13)$$

and

$$n_{\text{red}}(r) \propto \begin{cases} \left(\frac{r}{3.3 \text{ kpc}}\right)^{-1} \left(1 + \frac{r}{3.3 \text{ kpc}}\right)^{-2}, & r < 125 \text{ kpc}, \\ \left(\frac{r}{560 \text{ kpc}}\right)^{-1} \left(1 + \frac{r}{560 \text{ kpc}}\right)^{-2}, & r > 125 \text{ kpc}. \end{cases} \quad (14)$$

The projections of these best-fit models are drawn as the thick, dashed lines in Figure 12. Their absolute normalization is again unimportant for us, although their relative normalization does matter. This has been set so that $n_{\text{blue}}/n_{\text{red}} \rightarrow 4$, independent of radius in the limit $r \rightarrow \infty$. The projected sum of these red and blue models is shown in Figure 12 as the thin solid line, which is reasonably compatible with the completely independent projection of $n_{\text{tot}}(r)$ from equation (12).

With specifications for the Virgo mass profile $M_{\text{tot}}(r)$ and for the density profiles $n_{\text{cl}}(r)$ of the total, blue, and red GCSs thus in hand, we solve equations (8)–(10) for five different spatially constant values of the GCS orbital anisotropy β_{cl}^{22} :

$$\beta_{\text{cl}} \equiv \begin{cases} 0.99 & \left(\frac{\sigma_\theta^2}{\sigma_r^2} = 0.01, \text{ radial bias}\right), \\ 0.4 & \left(\frac{\sigma_\theta^2}{\sigma_r^2} = 0.6, \text{ radial bias}\right), \\ 0 & (\sigma_\theta = \sigma_\phi = \sigma_r, \text{ isotropic}), \\ -0.4 & \left(\frac{\sigma_\theta^2}{\sigma_r^2} = 1.4, \text{ tangential bias}\right), \\ -99 & \left(\frac{\sigma_\theta^2}{\sigma_r^2} = 100, \text{ tangential bias}\right). \end{cases} \quad (15)$$

Figures 13–15 show the results of this exercise applied to our three GCS samples. In each figure, the top panel shows the observed $\sigma_p(R)$ profile computed by smoothing the data with a radial kernel of fixed width $120'' \simeq 8.2 \text{ kpc}$ (rather than the $90''$ used for Fig. 6). Also shown are the 90% confidence bands, obtained by bootstrapping as described in § 3. The bottom panels show the aperture velocity dispersion and bootstrap estimates of the 90% confidence bands for the cluster color ranges indicated. Overlaid on the data in every case are the model curves predicted by substituting equations (11)–(15) in equations (8)–(10). We emphasize that these theoretical velocity dispersion profiles have not been fitted to the data: with $M_{\text{tot}}(r)$, $n_{\text{cl}}(r)$, and β_{cl} all specified a priori, there are no additional parameters to be adjusted. Note that the rising velocity dispersion profile seen in Figure 6 is once again evident here, not only in the measured $\sigma_p(R)$ and $\sigma_{\text{ap}}(R)$ profiles but also in the models. This predicted rise in $\sigma_p(R)$ and $\sigma_{\text{ap}}(R)$ comes about because the background mass density profile given by equation (11), and shown in Figure 10, is shallower at these radii than that of an isothermal sphere.

It is clear from Figure 13 that the M87 GCS as a whole has an almost perfectly isotropic velocity ellipsoid. Models with even modest amounts of anisotropy, $\beta_{\text{cl}} = \pm 0.4$, produce noticeably inferior matches to observed velocity dispersions, while strongly tangentially biased orbits ($\beta_{\text{cl}} = -99$) can be ruled out with greater than 90% confidence, and very radial orbits ($\beta_{\text{cl}} = 0.99$) are altogether out of the question. However, if the cluster sample is divided on the basis of metallicity, some interesting differences emerge. Figure 14 suggests a modest tangential bias in the metal-poor clusters, with $\beta_{\text{cl}} \sim -0.4$ at small radii (corresponding to $\sigma_\theta \sim 1.2\sigma_r$), perhaps tending toward isotropy at larger radii ~ 20 – 30 kpc . The opposite result is seen for the metal-rich GCs, which have a slight radial bias of roughly the same magnitude: Figure 15 suggests $\beta_{\text{cl}} \sim 0.4$, and thus $\sigma_\theta \sim 0.8\sigma_r$. This is just what is needed, of course, to balance the anisotropy in the blue GCS and produce the isotropy indicated for the combined sample in Figure 13. Qualitatively speaking, these contrasting anisotropies are also what might have been expected a priori, given the fact that the blue GCS has a much shallower density profile than the red subsystem, even though the two populations are embedded

²² It is worth emphasizing that these values of β_{cl} are best interpreted as density-weighted averages as a result of our assumption of spatially constant anisotropies.

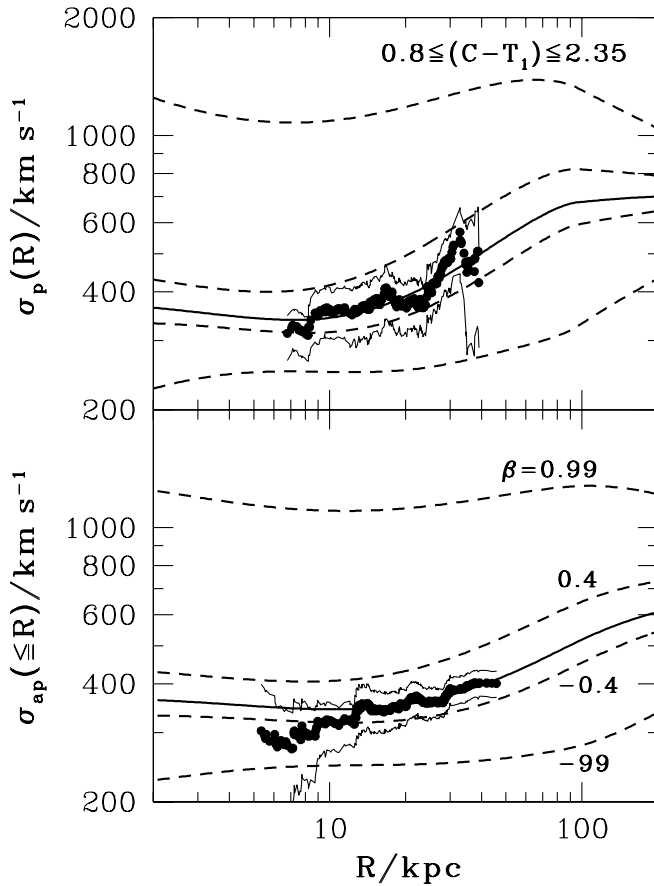


FIG. 13.—*Upper Panel*: Velocity dispersion profile for the complete sample of GCs. Circles represent biweight estimates for the line-of-sight velocity dispersion in radial bins of width $\Delta R = 120'' \simeq 8.7$ kpc; thin solid curves show bootstrap estimates of the 90% confidence limits on these measurements. The thick solid line shows the predicted velocity dispersion profile for a system of test particles that are embedded in the potential defined by eq. (11), follow a density profile given by eq. (12) (*thick, dashed line* in Fig. 11), and have an isotropic velocity ellipsoid ($\beta_{cl} \equiv 0$). From top to bottom, the four dashed curves show the predicted velocity dispersion profiles for $\beta_{cl} \equiv 0.99$ (a strong radial bias), $\beta_{cl} \equiv 0.4$ (a moderate radial bias), $\beta_{cl} \equiv -0.4$ (a moderate tangential bias), and $\beta_{cl} \equiv -99$ (a strong tangential bias). *Lower Panel*: Aperture velocity dispersion profile for the complete sample of GCs, with bootstrap estimates of the 90% confidence limits illustrated by thin solid lines. The thick solid curve shows the predicted aperture velocity dispersion profiles for the case of isotropic orbits, while the four dashed curves show model predictions with the same velocity anisotropies as in the above panel.

in the same gravitational potential and show no significant differences in their projected kinematics (see Fig. 6).

Romanowsky & Kochanek (2001) have derived a $\beta_{cl}(r)$ profile for the total GCS, i.e., they did not separate their velocity sample on the basis of metallicity. At small radii, the implied β_{cl} is markedly negative, thereby implying a substantial tangential bias for the GCS. However, this claim ultimately rests on their assumption that the background potential of M87/Virgo is distributed as a singular isothermal sphere, $M_{tot}(r) \propto r$, whereas the true $M_{tot}(r)$ in the core of Virgo is well constrained (principally by X-ray data; see Nulsen & Böhringer 1995; McLaughlin 1999a; see also Fig. 10) to grow substantially more rapidly than this with increasing radius. Said another way, the density distribution of the gravitating mass in the core of Virgo is significantly shallower than the $\rho \propto r^{-2}$ distribution of an isothermal sphere, and therefore the density distribution of

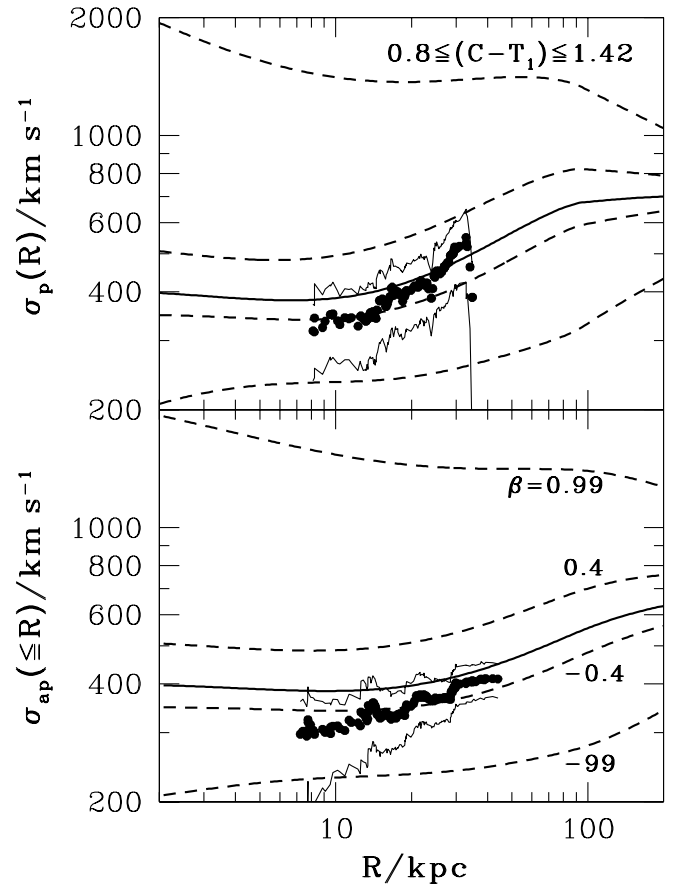


FIG. 14.—Same as Fig. 13, except for the sample of metal-poor (blue) GCs. Note that the aperture velocity dispersion at small radii in the lower panel falls below that expected in the case of isotropic orbits, at the 90% confidence level. The model that best matches the measured profile has $\beta_{cl} \simeq -0.4$, corresponding to a tangential bias of $\sigma_\theta \simeq 1.2\sigma_r$.

the central GCS does not require so large a tangential bias as Romanowsky & Kochanek (2001) found necessary to satisfy the Jeans equation.

Finally, we consider the effect on our results if our adopted extrapolation of the GCS density profiles in Figure 12 and equations (12)–(14) is somehow in error. It seems unlikely that the GC distribution could become shallower than the hot intracluster gas (and the dark matter) in Virgo, and thus Figures 16 and 17 explore the implications of an $n_{cl}(r)$ that drops off very steeply toward large radii. Rather than requiring $n_{cl}(r) \propto \rho_{gas}(r)$ at the unobserved $r \gtrsim 100$ kpc, then, we take at face value simple fits to our CT_1 density profiles for $5 \lesssim R \lesssim 30$ kpc and assume

$$n_{blue}(r) \propto \left(\frac{r}{21.3 \text{ kpc}}\right)^{-1} \left(1 + \frac{r}{21.3 \text{ kpc}}\right)^{-2}, \quad \text{all radii} \quad (16)$$

and

$$n_{red}(r) \propto \left(\frac{r}{3.3 \text{ kpc}}\right)^{-1} \left(1 + \frac{r}{3.3 \text{ kpc}}\right)^{-2}, \quad \text{all radii} . \quad (17)$$

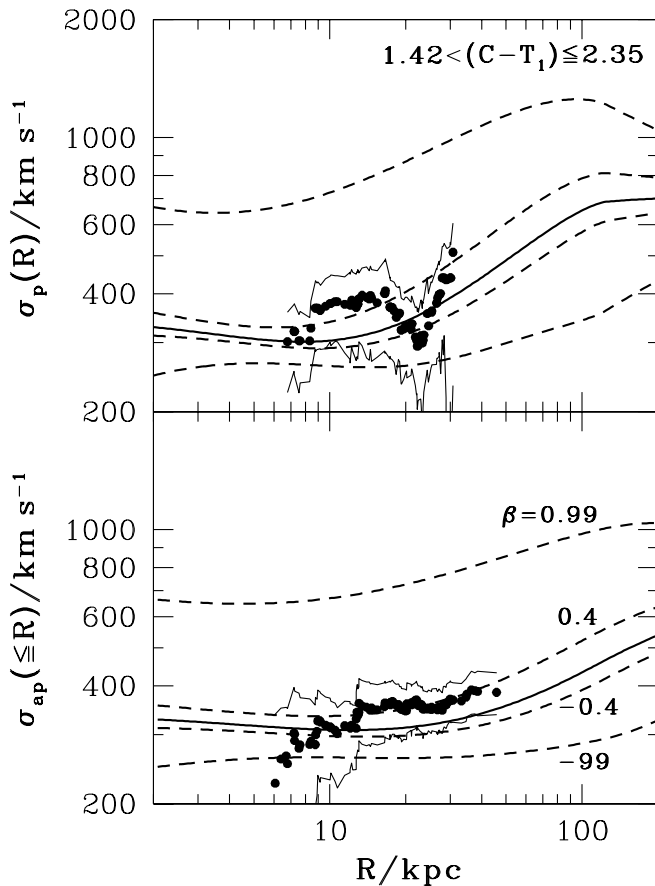


FIG. 15.—Same as Fig. 13, except for the sample of metal-rich (red) GCs. In this case, the aperture velocity dispersion profile at large radii in the lower panel lies above that expected for an isotropic velocity ellipsoid. A model that reasonably matches the measured profile has $\beta_{\text{cl}} \approx 0.4$, corresponding to a radial bias of $\sigma_{\theta} \approx 0.8\sigma_r$.

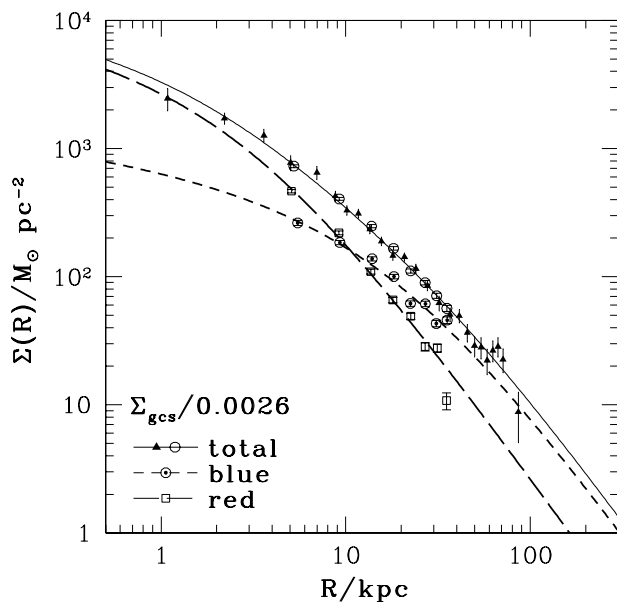


FIG. 16.—Alternate extrapolation of the red and blue GCS density profiles to larger, unobserved radii (cf. Fig. 12). Thin, solid line is the sum of the red and blue fits (thick lines) and is in good agreement with the independently observed density profile of the full GCS.

The thick, dashed lines in Figure 16 compare the projection of these functions to the same data considered in Figure 12. The thin, solid line, which shows the sum of the red and blue projected densities, is again in good agreement with the independently observed density distribution of the full GCS.

We use these new density profiles with the same $M_{\text{tot}}(r)$ from equation (11) and the same five constant β_{cl} values from equation (15) to compute new models for the $\sigma_p(R)$ and $\sigma_{\text{ap}}(\leq R)$ of the metal-poor and the metal-rich components of the GCS. Figure 17 compares these to the data, which again have been smoothed with a $120''$ wide sliding radial bin and are shown with bootstrap estimates of their 90% confidence bands. Because the large- r density gradient of both cluster subsystems has been made steeper by hypothesis without changing any other aspect of the dynamical models, the data would appear now to suggest a move toward substantial radial bias in orbits of both blue and red clusters at the largest radii covered here. We stress, however, that we regard this particular scenario as a very extreme possibility, as the GCS density profiles postulated earlier are certainly closer to the truth. For instance, if $n_{\text{cl}}(r)$ indeed behaves as in Figure 16 rather than as in Figure 12, then we must conclude that the GC-to-baryon mass ratio of 0.0026 is only coincidentally realized, and then over a limited range of radius, in M87, even though this “universal” ratio matches precisely what is found by McLaughlin (1999b) for nearly 100 other early-type galaxies. In any case, Figure 17 also shows that the GC volume density profiles cannot fall off more rapidly than roughly $n_{\text{cl}} \propto r^{-3}$, since this gradient already requires the clusters at large r to have nearly purely radial velocity ellipsoids in order to reproduce the observed line-of-sight velocity dispersion.

5. DISCUSSION

5.1. Results for Other Ellipticals from Globular Clusters

Before turning our attention to the various models that have been proposed for the formation of GCSs and their host galaxies, we pause first to compare our findings for the GCS of M87 with those of other elliptical galaxies. Perhaps the most natural comparison is that of M49, the most luminous member of the Virgo Cluster, whose GCS has been studied recently by Sharples et al. (1998) and Zepf et al. (2000). From a sample of 144 GCs with measured velocities, Zepf et al. (2000) report that the metal-poor and metal-rich GCSs have different dynamical properties, i.e., $v_{\text{rot}}/\sigma \sim 0.3$ and 0.1 , respectively (with $v_{\text{rot}}/\sigma < 0.56$ and 0.34 at 99% confidence). These estimates are to be compared with the value of $v_{\text{rot}}/\sigma \sim 0.45$, which we measure for both components in M87. Hui et al. (1995) have analyzed the radial velocities of 433 planetary nebulae (PNs) and 62 GCs in NGC 5128 and conclude that the metal-rich GCs in that galaxy show roughly the same dynamical properties as do the PNs, $v_{\text{rot}}/\sigma \sim 0.3$, whereas the metal-poor GCs show no evidence of rotation. Meanwhile, Kissler-Patig et al. (1999) find some marginal evidence for rotation among the outermost GCs in NGC 1399, the central elliptical in Fornax, but as a result of the limited size of their radial velocity sample, they were unable to ascertain if the chemically distinct GC populations differ in their dynamical properties. Thus, at this early stage, no obvious pattern in the dynamical properties of the GCSs of elliptical galaxies has yet emerged.

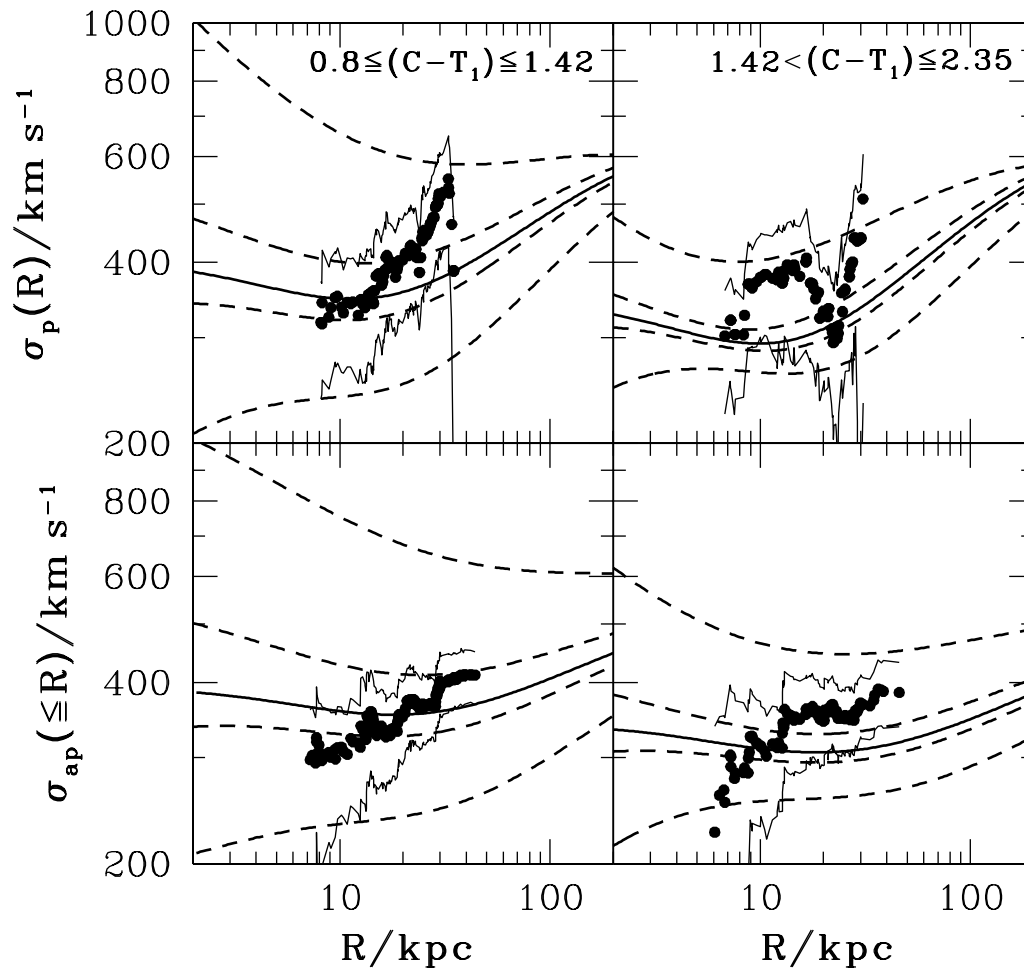


FIG. 17.—Model vs. observed dispersion profiles, shown separately for the blue and red subsets of the M87 GCS, assuming the alternate density profiles shown in Fig. 16 and described by eqs. (16) and (17). Since the mass profile of M87/Virgo is fixed in this analysis, the data in this case prefer models with stronger radial bias in the GCS orbits at large galactocentric radii. Curves shown have constant $\beta = 0.99, 0.4, 0, -0.4,$ and -99 , as in Figs. 13–15.

5.2. Results for Other Ellipticals from Planetary Nebulae

Radial velocity surveys of PNs represent an alternative, and complementary, method of studying the halo dynamics of giant elliptical galaxies. While there have been no dynamical studies of the PN population of M87 itself, some comparisons are possible for the three luminous early-type galaxies having large numbers of measured PN radial velocities: NGC 5128 (Hui et al. 1995), NGC 4406 (Arnaboldi et al. 1996), and NGC 1316 (Arnaboldi et al. 1998). The PNs in all three galaxies show evidence for significant rotation, $v_{\text{rot}}/\sigma \sim 0.5$ – 1 , in their outer regions. In this respect, these galaxies resemble M87, which has $\langle (\Omega R)/\sigma \rangle \sim 0.5$ from its GCS, with some evidence for slightly lower values in the inner regions of the galaxy and an outward increase in $(\Omega R)/\sigma$. Moreover, integrated-light spectroscopy in the inner regions of these galaxies reveals little or no rotation in each case, similar to the situation for luminous elliptical galaxies, and for M87 in particular (e.g., $v_{\text{rot},*}/\sigma_* \lesssim 0.1$; Davies & Birkinshaw 1988). On the other hand, none of these galaxies have the generally round and smooth photometric appearance of M87: NGC 5128 and NGC 1316 are clear examples of recent gas-rich mergers or accretions (e.g., Schweizer 1980), and NGC 4406 is probably best classified as an S0 galaxy (Arnaboldi et al. 1996). While

firm conclusions must await the measurement of radial velocities for PNs in the vicinity of M87, our results for the M87 GCS appear consistent with the claim of Arnaboldi et al. (1998) that giant elliptical galaxies, by virtue of their relatively rapid rotation at large radii, may contain roughly as much angular momentum per unit mass as do spiral galaxies assuming that the GC and PN kinematics are representative of the kinematics of the underlying galaxy mass.

5.3. The GCS Velocity Ellipsoid at Small Galactocentric Radii

It has been known for some time that the surface density profile of the GCs surrounding M87 exhibits a “core” of radius $R_c \simeq 4$ – 5 kpc (Lauer & Kormendy 1986; McLaughlin 1995). The possibility that this core developed as a result of GC destruction through tidal shocks from a central bulge or black hole, or from an underlying triaxial potential, has been explored by many investigators (e.g., Ostriker, Binney, & Saha 1989; Pesce, Capuzzo-Dolcetta, & Vietri 1992). These authors also noted that such processes are expected to lead to a preponderance of tube orbits among the surviving GCs relative to the initial sample. Moreover, in the specific case of the Galactic GCS, Murali & Weinberg (1997) have shown that GCs on eccentric orbits will undergo the most rapid relaxation and evaporation due to

enhanced tidal heating; the preferential destruction of such clusters will therefore lead to an orbital distribution that becomes more tangentially biased with time. Thus, depending of course on the initial shape of the GCS velocity ellipsoid, the tangential bias that we find for the GCs at small galactocentric radii, especially within an effective radius (see Figs. 13–15), may provide evidence that these dynamical processes have played a role in shaping the presently observed GCS.

5.4. Cooling Flow Models

Fabian, Nulsen, & Canizares (1984) were the first to propose that the populous GCSs associated with some cD galaxies might be the signature of GC formation through cooling flows from their X-ray halos. A number of difficulties with this scenario have been raised over the years, e.g., most “high- S_N ” and/or cooling flow galaxies show no evidence for young clusters, the GCs are generally more metal-deficient than the intracluster gas, and it is unclear how the cooling gas might condense into clumps of mass $\sim 10^5 M_\odot$. For M87, which is both an incipient cD galaxy and the prototypical “high- S_N ” system, we may now add another difficulty to this list: as described in § 4, the orbits of the surrounding GCs are closely isotropic, not the radial orbits expected if the GCs have condensed out of the infalling gas. As Figures 13–15 demonstrate, purely radial orbits are ruled out at very high significance by our observations. Thus, it appears highly unlikely that a large fraction of M87’s GCs could have formed by mass dropout from a cooling flow.

5.5. Monolithic Collapse Models

Can the relatively rapid rotation of the M87 GCS be accommodated within the context of formation models that argue for the monolithic collapse of a single protogalactic gas cloud? Like those of most other giant elliptical galaxies, the M87 GCS is disjoint in terms of its chemical properties (i.e., the GC metallicity distribution function is decidedly bimodal; Whitmore et al. 1995; D. Geisler et al. 2001, in preparation; see also Fig. 1), and this observation alone provides a compelling argument against the monolithic collapse picture. Figures 7–9 may provide additional evidence against this model: both the metal-poor and metal-rich GC subsamples exhibit significant rotation, with $\Omega R \simeq 170 \text{ km s}^{-1}$ and $\langle(\Omega R)/\sigma_p\rangle = 0.45$. In monolithic collapse scenarios, the angular momentum of galaxies can only arise from tidal torques from companions (Peebles 1969). A common measure of a galaxy’s angular momentum content is the dimensionless spin parameter, $\Lambda = J|E|^{1/2}G^{-1}M^{-1/2}$, where J , E , and M are the angular momentum, binding energy, and mass of the collapsed galaxy. Fall (1979) showed that, for an elliptical galaxy in gravitational equilibrium, $\Lambda \sim 0.3\langle(\Omega R)/\sigma_p\rangle$. Thus, the inferred spin parameter of the M87 GCS is $\Lambda \simeq 0.15$, which is lower than, but still consistent with, the value of $\Lambda \simeq 0.18$ found by Kissler-Patig & Gebhardt (1998) from a smaller sample of GCs. This spin parameter is roughly twice that expected from analytical and numerical simulations of the collapse of a single, isolated protogalactic cloud (Peebles 1969; Efsthathiou & Jones 1979). It is, however, worth bearing in mind that M87 is by no means an isolated system. Perhaps a more severe obstacle for such models is the abrupt shift in the orientation of the rotation axis for the metal-poor GC

subsample at $R \simeq 16\text{--}18 \text{ kpc}$. If real, this feature would be difficult to explain in models where M87 and its GCS formed via the collapse and spin-up of a single protogalactic cloud.

5.6. Merger and Accretion Models

Two variations on the general theme of mergers and accretions have been proposed for the formation of GCSs: (1) major mergers involving a pair of gas-rich disk galaxies (each containing only metal-poor GCs), which result in the formation of new, metal-rich GCs (Ashman & Zepf 1992); and (2) hierarchical growth of a preexisting “seed” galaxy (containing its own metal-rich GCS) through the accretion of numerous smaller galaxies or protogalactic fragments that harbor predominantly metal-poor GCs (Côté et al. 1998). We discuss the viability of these two models in light of the dynamical evidence presented above.

We begin by reiterating the well-established result that mergers of purely stellar disks are a highly unlikely mechanism for the production of giant elliptical galaxies. Both N -body simulations (e.g., Barnes 1992; Hernquist 1992) and simple arguments regarding central phase-space densities (Carlberg 1986) have demonstrated that the end products of such mergers have cores that are far more diffuse than the centers of giant elliptical galaxies. In addition, luminous elliptical galaxies typically have Hubble types of E2 (Franx, Illingworth, & de Zeeuw 1991), whereas the end products of pairs of stellar disks are frequently more elongated, with Hubble types of E3–E7 (Hernquist 1992).²³ Finally, the merger end products often show large misalignments between their rotation and minor axes (Barnes 1992; Weil & Hernquist 1994, 1996; Heyl et al. 1996). From an observational perspective, such large misalignments are rare: Franx et al. (1991) find much smaller misalignments for the majority of giant elliptical galaxies based on long-slit spectroscopy of their integrated light.

There are various ways to surmount some or all of these difficulties within the context of the merger hypothesis: (1) the stellar disks may initially harbor compact bulges with high phase-space densities (Hernquist 1993); (2) the disks may contain significant amounts of gas (Barnes & Hernquist 1996); or (3) ellipticals may be the result of multiple, dissipationless mergers (Weil & Hernquist 1994, 1996). From a purely philosophical perspective, the first option is obviously unsatisfactory given that the initial conditions for spiral-spiral mergers require a significant fraction of the initial mass to reside in compact, dynamically hot components. In the words of Hernquist (1993), “It seems likely that even the most strident critics of the merger hypothesis would admit the possibility that mergers of small ellipticals will yield big ellipticals.”

The second alternative, that giant ellipticals form during dissipative mergers of pairs of stellar disks, each of which contains significant gas components, is closely related to the Ashman & Zepf (1992) model for the formation of GCSs in giant elliptical galaxies. In the specific case of M87, the most compelling piece of evidence for a past major merger is the possible flip in the position angle of the rotation axis for the metal-poor GCS; we caution, however, that this interpretation of the observed discontinuity is not unique (see § 5.7).

²³ M87 itself has a Hubble type of E2 (van der Marel 1991), though the ellipticity does increase outward, reaching a maximum of E4 in the cD envelope (see Fig. 18).

As a further complication, the uncertainties involved in correctly modeling the effects of gas cooling, feedback, and star formation in dissipational spiral-spiral simulations are formidable. To date, the most detailed study of merging galaxies to include gasdynamical effects is that of Barnes & Hernquist (1996), who approximated the interstellar medium as an incompressible fluid. They found that the inclusion of a gaseous component has a dramatic effect on the properties of the merger end products and may alleviate some of the problems described above for the case of purely stellar mergers, i.e., including gas leads to merger remnants that have somewhat higher central densities, and it may also produce closer alignments between the angular momenta and minor axes. These conclusions, however, are highly dependent on how the gas is assumed to cool (see, e.g., Mihos & Hernquist 1994; Barnes & Hernquist 1996, § 4.3).

Simulations of merging stellar disks have shown that the angular momentum axes of the merger remnants often show large misalignments with the minor axes. At large radii, metal-poor and metal-rich GCSs in M87 both rotate around axes that are closely aligned with the minor axis. If the GCs are accurately tracing the kinematics of the underlying galaxy mass, this alignment may constitute a difficulty for the major merger model; that is to say, such a small misalignment in the merger remnant is by no means implausible in the major merger model, but neither is it predicted. In their simulations of gas-free mergers of equal-mass disks, Heyl et al. (1996) find the distribution of misalignment angles to be nearly flat, with occasional misalignments of 75° or 80° although, as mentioned above, gas may play a role in ameliorating these large misalignments.

It is clear that additional research into the influence of gas on the nonaxisymmetry of merger remnants is needed urgently. Moreover, it is important to quantify the expected angular momentum content and rotational properties of any stars or GCs that might form during dissipational mergers. In the case of M87, both the metal-poor and metal-rich samples show significant rotation, with $\langle(\Omega R)/\sigma_p\rangle \sim 0.45$. This value is intermediate to the disparate values of $\langle(\Omega R)/\sigma_p\rangle \sim 1$ (Côté 1999) and $\langle(\Omega R)/\sigma_p\rangle \sim 0.1$ (Zepf et al. 2000) observed for the metal-rich GCs belonging to the Milky Way and NGC 4472, respectively. However, the metal-rich GCs in both of these galaxies have been identified as the end products of gas-rich mergers (i.e., Ashman & Zepf 1992 and Zepf & Ashman 1993 for the Milky Way; Zepf et al. 2000 for NGC 4472).

In the dissipationless hierarchical growth scenario, the simulations of Weil & Hernquist (1994, 1996) indicate that the rotation axis of the merger remnant is expected to be more closely aligned with the photometric minor axis.²⁴ Strictly speaking, these simulations, which do not include gas, apply to merger remnants of small virialized groups of galaxies, although the generic kinematic properties of the end products are similar to those found in cosmological simulations of galaxy formation through the hierarchical agglomeration of smaller galaxies and protogalactic fragments (Barnes & Efstathiou 1987; Frenk et al. 1988; Quinn

& Zurek 1988; Warren et al. 1992; cf. Dubinski 1998). In general, the assumed initial conditions would be appropriate if centrally dominant galaxies such as M87 are the result of mergers of small subgroups that later coalesced into larger structures, as originally suggested by White (1982). The end products of these simulations appear nearly round in most projections and exhibit small kinematic misalignments when integrated over the full range in radius. Near their centers they show relatively little rotation, but they can rotate rapidly in their outer regions, with $0 \lesssim v_{\text{rot}}/\sigma \lesssim 0.8$, although this conclusion is likely to depend on the assumed orbital properties of the progenitor galaxies (Dubinski 1998).

In short, these results are broadly consistent with the observed behavior of the metal-poor GCS in M87, but the poorly constrained rotation curve at large radii makes definite conclusions impossible. There is also some evidence that the inferred rotation of the M87 GCS (particularly that of the metal-poor component) may include a contribution from large-scale streaming motions along the Virgo principal axis (see below). And while the simulations of Weil & Hernquist (1996) produce end products with low triaxialities and roughly oblate shapes (consistent with the results of dynamical modeling of the line-of-sight velocity profile in the inner regions of M87; e.g., van der Marel 1991, 1994; Bender, Saglia, & Gerhard 1994), it is important to bear in mind that the N -body simulations, though similar in some respects to the hierarchical growth model of Côté et al. (1998), are not completely analogous. Most notably, the N -body simulations do not include a single dominant progenitor galaxy, whereas in the agglomeration picture of Côté et al. (1998), the metal-rich clusters arise in the dissipative (monolithic) collapse of this component.

A more definitive test of these scenarios will require a crucial piece of evidence that is currently lacking: accurate age estimates for the metal-rich and metal-poor GCs. To date, the limited observational evidence has proven inconclusive. Kundu et al. (1999) argued, on the basis of broadband VI photometry, that the metal-rich GCs in M87 are 3–6 Gyr younger than their metal-poor counterparts, as expected in the major merger model. However, this claimed age difference is roughly the same size as the uncertainties involved in using broadband VI colors to derive GC ages and is in contradiction with the findings of Cohen et al. (1998), who, from Keck spectroscopy of the brightest clusters in M87, found the metal-rich and metal-poor GC populations to be both old and coeval (i.e., $T \sim 13$ Gyr).

The principal obstacle to understanding the merger/accretion history of M87 remains the uncertain role played by gas. From a theoretical point of view, improved numerical simulations that include gasdynamical effects and star formation are needed urgently. On the observational front, it is important to measure the star formation history of the GCS directly, through improved age estimates for the chemically distinct GC populations (e.g., A. Jordan et al. 2001, in preparation).

5.7. Connection to the Virgo Cluster on Larger Scales

It has long been known that the brightest of Virgo's giant elliptical galaxies define a remarkably linear pattern on the plane of the sky (Arp 1968). It was recently shown that this extended arrangement, which passes through the cluster core at a position angle of 110° – 125° and is roughly centered on M87, is the projection of a highly collinear, three-

²⁴ Direct evidence that this process has played a role in the formation and evolution of M87 has been presented by Weil, Bland-Hawthorn, & Malin (1997), who identified a diffuse plume of stellar material at large radii, the likely result of the accretion of a small satellite galaxy.

dimensional filament: the so-called principal axis of the Virgo Cluster (West & Blakeslee 2000). Thus, the rotation axis of the M87 GCS not only coincides with the galaxy's minor axis at large galactocentric radii but also is roughly aligned with the minor axis of the surrounding cluster. It is then natural to ask if some fraction of the GCS around M87 may somehow be associated with Virgo itself (White 1987; West et al. 1995). One mechanism that might give rise to such a population of “intracluster” GCs is their acquisition from other galaxies by tidal stripping (White 1987; West et al. 1995). Another is the possible formation of GCs in “failed dwarfs” throughout Virgo: low-mass, loosely bound clouds of gas (analogous to, but rather more isolated than, the protogalactic fragments thought to form stars and GCs in most large galaxies; see, e.g., Harris & Pudritz 1994; Côté et al. 1998, 2000) that formed normal complements of (generally metal-poor) GCs but were then destroyed before much further star formation occurred, perhaps as a result of galactic winds driven at least in part by the GC formation itself (Harris et al. 1998; McLaughlin 2000). Whether or not the numbers of any such clouds were enhanced in Virgo through cold dark matter biasing of either the GCs (West 1993) or their host protogalactic fragments (see Ferguson & Binggeli 1994), the plausible result could have been an addition to the intracluster medium of GCs and hot gas that eventually settled naturally to the bottom of the cluster's potential well, i.e., directly around M87.

The evidence in support of such a connection between the M87 GCS and the Virgo Cluster can be summarized as follows. First, like all cD galaxies, M87 possesses an extended, low surface brightness envelope, and much evidence exists that such envelopes are entities quite distinct from cD galaxy cores. For instance, these galaxies obey the D_n - σ relation defined by normal ellipticals only after the luminosity excess above an $R^{1/4}$ -law fit to the surface brightness profile of the interior is excluded (Tonry 1987); the total luminosity of cD envelopes correlates with several cluster properties including cluster richness and X-ray luminosity; the surface brightness profiles of the envelopes obey density profiles that roughly match that of the galaxies in their parent clusters (Schombert 1988); and the ellipticity and position angle of the galaxy isophotes often show dramatic discontinuities at the radius where the envelope begins to dominate the surface brightness profile. The latter issue is particularly germane in the case of M87. McLaughlin, Harris, & Hanes (1993, 1994) showed that the GCS itself exhibits a sharp jump in surface density that coincides with the onset of the stellar cD envelope and that the ellipticity and orientation of the GCS roughly match that of the underlying envelope. Moreover, as was described in § 4, the so-called excess of GCs at large radii in M87 is now recognized to be not a genuine surfeit but a consequence of the fact that the GCS-to-baryon mass ratio there has the same value, $\rho_c(r)/[\rho_{\text{gas}}(r) + \rho_{\text{stars}}(r)] = 0.0026$, that is exhibited by nearly 100 other galaxies (McLaughlin 1999b). Since the stellar component of M87 dies out relatively rapidly beyond $r \gtrsim 50$ kpc (e.g., Fig. 11), the natural interpretation is that the distant GCs are associated with the X-ray gas around M87; and that gas is itself at the virial temperature of the Virgo Cluster dark matter halo (see, e.g., McLaughlin 1999a).

The dynamical analysis presented in this paper adds to this line of argument. In particular, it is noteworthy that the position angle of the rotation axis of the metal-poor GCs

shows an apparent discontinuity close to the onset of the cD envelope. To aid in the visualization of this discontinuity, Figure 18 shows the orientation of the angular momenta axes of metal-poor and metal-rich GCs surrounding M87 overlaid on an image from the Palomar Digital Sky Survey. The blue and red arrows refer to the metal-poor and metal-rich GCs, respectively. The length of each arrow is proportional to the amplitude (ΩR) of the best-fit sine curve in radial bins of fixed width $\Delta R = 90'' \simeq 6.5$ kpc (see Fig. 8). The dotted yellow curves show the best-fit ellipses to the surface brightness profile of the galaxy, taken from Carter & Dixon (1978). The ellipse nearest the onset of the cD envelope is shown by the thick, dashed curve. Recall from § 4 that in the limit of $r \rightarrow \infty$, $n_{\text{blue}}/n_{\text{red}} \rightarrow 4$. Thus, the metal-poor component dominates the GCS at these radii, although both components (i.e., the metal-rich and the metal-poor cluster systems) appear to rotate around an axis that is roughly aligned with the minor axis of the large-scale structure in Virgo. At the largest observed radii, the rotation curve of the GCS approaches the circular velocity of Virgo itself (although the uncertainties in the fitted values of ΩR are large at these distances).

To examine the apparent rotation of the M87 GCS in more detail, and to explore the possible connections with bulk motions in the Virgo Cluster, we have generated two-dimensional maps of the GC velocity fields using the non-parametric technique described in Gebhardt et al. (1995) and Merritt, Meylan, & Mayor (1997). In this approach, the cluster-by-cluster velocity residuals about a mean, line-of-sight velocity are smoothed with a “thin-plate smoothing spline” that is chosen on the basis of a generalized cross-validation technique (Wahba 1990). The results of this exercise are presented in Figure 19. Panels (a)–(c) in this figure show smoothed velocity fields for the full sample of GCs, the metal-rich subsample, and the metal-poor subsample, respectively. A striking feature of Figure 19b is the form of the rotational field for the metal-rich GCs, i.e., it appears noncylindrical in nature, consistent with the discussion around equations (3)–(5) in § 3. Rather, the rotation field shows a “double-lobed” pattern with maxima at $R \sim 3.5R_e - 4R_e$ (25–30 kpc) along the approximate photometric major axis of the galaxy, although additional radial velocities may be needed to characterize fully the true two-dimensional rotation field. Figure 19c suggests that the rotation field of the metal-poor GCS may more closely resemble that of a solid body; or, alternatively, it may show evidence for a “shear” in the line-of-sight velocity. The magnitude and orientation of this putative shear are apparent in Figure 19d, which shows the plane of best fit to the velocity residuals for the metal-poor GCS. Interestingly, the sharp flip in the rotation axis of the metal-poor clusters seen in the previous figure is not obvious in this (smoothed) representation of the two-dimensional velocity field, although there does appear to be a local minimum in the rotation velocity due south of the galaxy's center at a distance of $R \sim 1.5R_e$ (7 kpc).

Based on the kinematics of dwarf galaxies and X-ray imaging, Binggeli (1999) has argued that the Virgo Cluster and particularly its dwarf galaxies are not yet in dynamical equilibrium. Rather, material appears to be infalling onto M87 along the principal axis of the Virgo Cluster. It is notable that this axis passes through both M87 and M86; each of these supergiant elliptical galaxies is embedded in a swarm of dwarf elliptical galaxies and thereby defines a

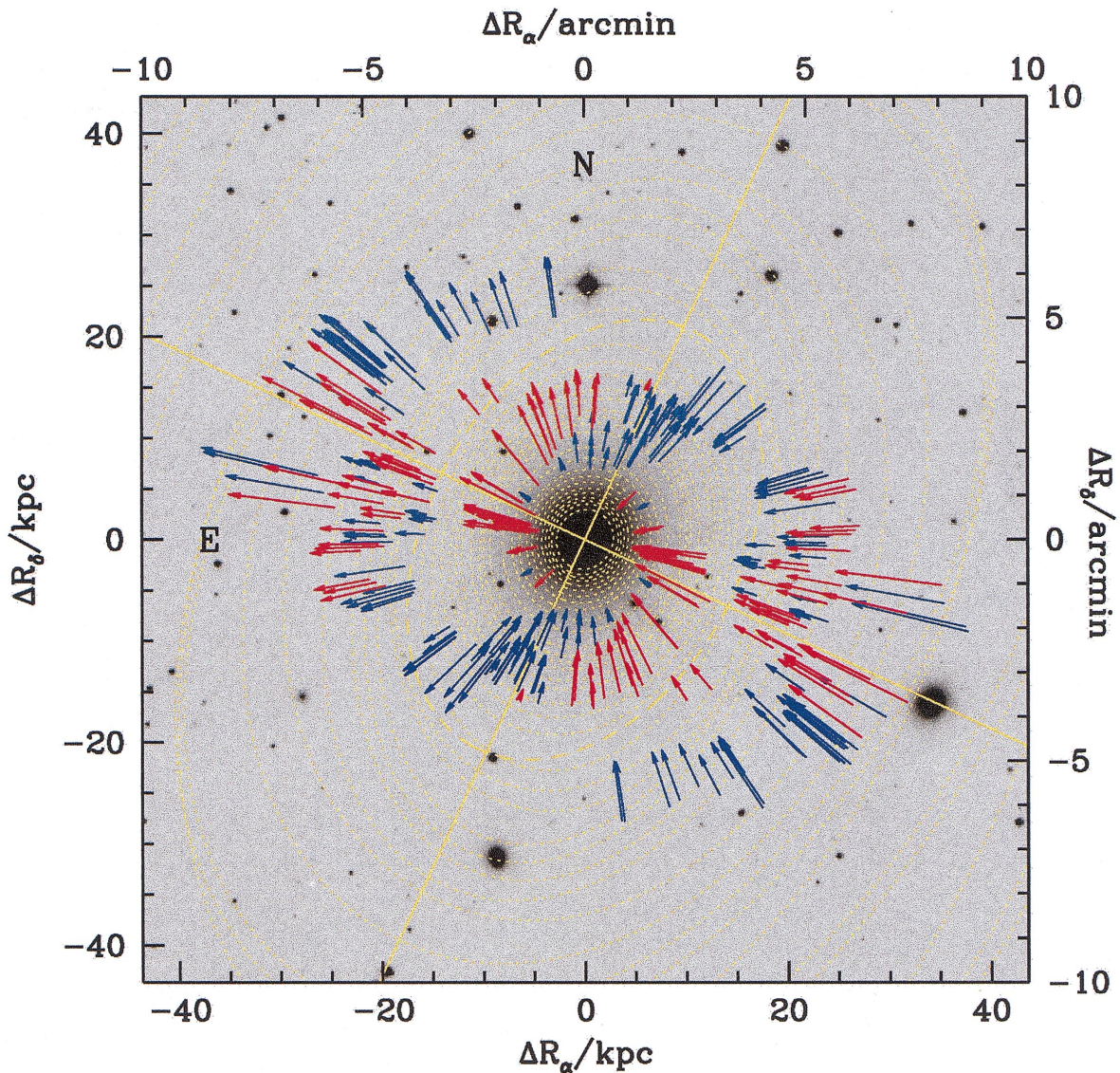


FIG. 18.—Orientation of the angular momenta axes of metal-poor and metal-rich GCs surrounding M87 (blue and red arrows, respectively) overlaid on an image from the Palomar Digital Sky Survey. A fixed radial bin width of $\Delta R = 90'' \simeq 6.5$ kpc has been adopted throughout. The length of each arrow is proportional to the amplitude of the best-fit sine curve in each annulus. The maximum positive rotation velocity at each radius is found 90° counterclockwise of the direction indicated by the arrows. The image measures $20' \times 20'$ on a side, or 87.3×87.3 kpc for our adopted M87 distance. The luminosity-weighted mean photometric minor and major axes for the galaxy are indicated by the solid yellow lines. The dotted yellow curves indicate the best-fit ellipses to the surface brightness profile from Carter & Dixon (1978). The dashed ellipse indicates the approximate location and orientation of the galaxy's cD envelope.

major Virgo subcluster. It is therefore natural to ask if the kinematics of the GCS surrounding M87 is related to that of the more distant Virgo galaxies. Such a comparison is especially relevant to the notion that some fraction of the M87 GCS might be composed of the accreted and/or infalling remains of “failed dwarfs.”

In order to compare the large-scale kinematics of Virgo directly to that of the M87 GCS, we have carried out the same smoothing procedure described above for the Virgo Cluster galaxies. Using the NASA Extragalactic Database, we identified a sample of 117 galaxies that are located within 2° (525 kpc) of M87 and have measured radial velocities in the range $-1000 \leq cz \leq 3500$ km s $^{-1}$. The two-dimensional rotation field for this sample is shown in Figure 19e; the corresponding plane of best fit to the observed velocity residuals is shown in Figure 19f. Although the limited sample size makes firm conclusions impossible, it does appear that the Virgo galaxies show evidence for a

gradient in their line-of-sight velocity that is roughly in the same direction as that observed for the distant metal-poor GCs surrounding M87, broadly consistent with the infall picture.²⁵

Finally, we consider the one-dimensional velocity dispersion profile of the M87 GCS in the larger context of the surrounding Virgo Cluster. Figure 20 shows the measured and predicted GC aperture dispersion profiles from Figures 13–15, placed now on an expanded radial scale that also includes data for 246 early-type (mostly dE) Virgo galaxies from Girardi et al. (1996). Error bars on the latter measure-

²⁵ Note that the observed “shear” is probably not due to the projection of the Virgo space velocity onto the plane of the sky. The expected magnitude of this effect is $v_{\text{proj}} = v_s \sin \Omega$, where v_s is the cluster space velocity and $\Omega \simeq 0.3$ is the angle spanned by the GCs with measured velocities. Thus, for an assumed Virgo space velocity of $v_s = 2000$ km s $^{-1}$, $v_{\text{proj}} \sim 10$ km s $^{-1}$, far less than the size of the velocity gradient seen in Fig. 19d.

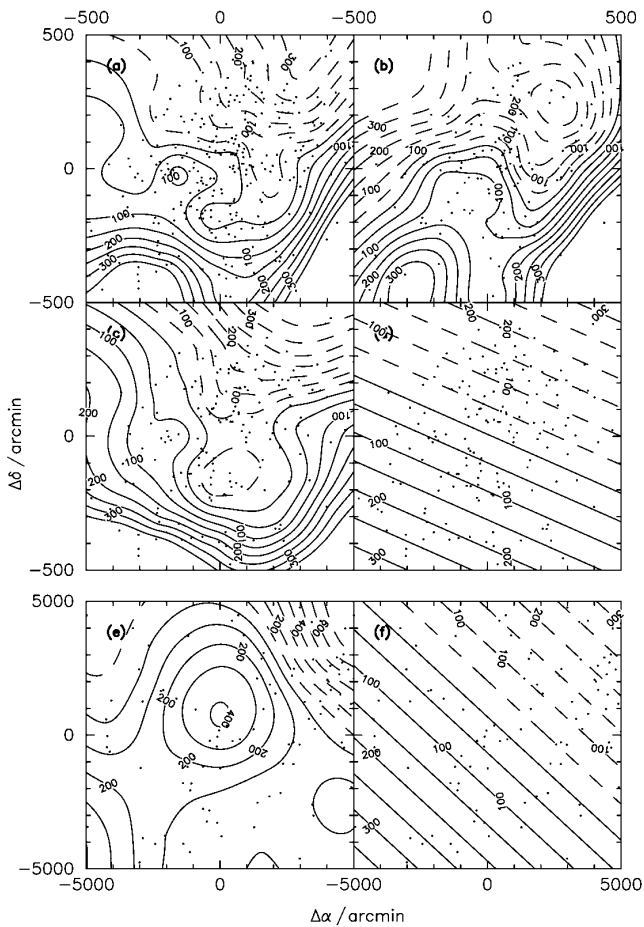


FIG. 19.—(a) Line-of-sight, rotational velocity field for the M87 GCS obtained using the full sample of 278 clusters with measured radial velocities (*dots*). North is up and east is to the left. Contours are labeled in km s^{-1} with respect to the mean velocity. Solid contours indicate positive velocities, while dashed contours indicate negative velocities. (b) Same as (a), except for the sample of 117 metal-rich (red) GCs. (c) Same as (a), except for the sample of 161 metal-poor (blue) GCs. (d) Plane of best fit to the rotational velocity field of metal-poor GCs. Contours are labeled in km s^{-1} with respect to the mean velocity. As in (a), solid contours indicate positive velocities, while dashed contours indicate negative velocities. (e) Line-of-sight, rotational velocity field for 117 Virgo galaxies located within 2° of M87 (*dots*). North is up and east is to the left. Contours are labeled in km s^{-1} with respect to the mean velocity. As in (a), solid contours indicate positive velocities, while dashed contours indicate negative velocities. (f) Plane of best fit to the rotational velocity field of Virgo galaxies located within 2° of M87. Contours are labeled in km s^{-1} with respect to the mean velocity. As in (a), solid contours indicate positive velocities, while dashed contours indicate negative velocities.

ments refer to 95% confidence limits. The three curves show the predicted σ_{ap} profiles corresponding to the GC subsystems and orbital anisotropies indicated in the lower right corner of the figure. Cases of purely radial orbits, $\beta = 1$, are not shown since all such models are ruled out at high confidence (see Figs. 13–15).²⁶ Given that the early-type galaxies in Virgo trace the cluster’s dark matter density profile

²⁶ Indeed, the fact that purely radial orbits are so strongly ruled out for the GCS as a whole suggests that any infall component of GCs on high-eccentricity orbits probably constitutes only a subsample of the overall system.

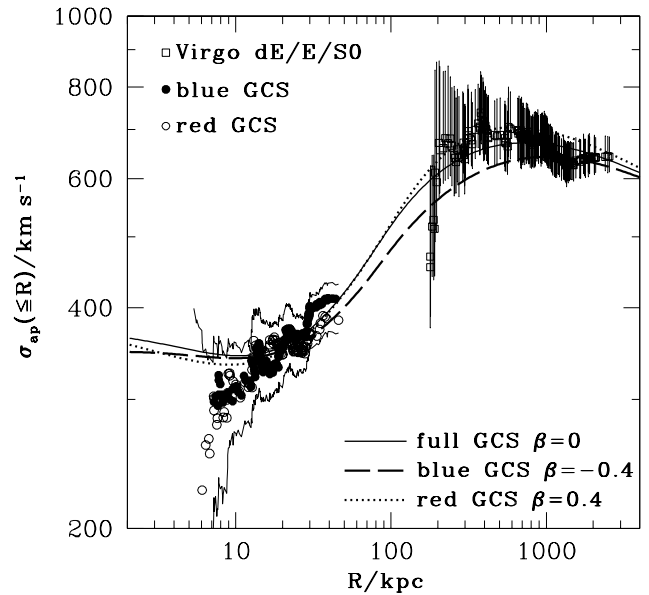


FIG. 20.—Aperture dispersion profiles of the metal-poor (blue) and metal-rich (red) GCs around M87 and of the early-type galaxies in the Virgo Cluster at large radii (data from Girardi et al. 1996, shown with 95% confidence limits as error bars). Curves are the full extent of the models for the blue GCS with a fixed orbital anisotropy of $\beta \equiv -0.4$ (cf. Fig. 14), for the red GCS with $\beta \equiv 0.4$ (cf. Fig. 15), and for the two subsamples combined with a fixed $\beta \equiv 0$ (cf. Fig. 13).

(McLaughlin 1999a), the striking match seen here between the kinematics of the GCs and the galaxies lends support to our earlier assertion (recall eqs. [12]–[14] and Fig. 12) that, in the limit of large galactocentric radius, the M87 GCS also traces the Virgo dark matter. Thus, the properties of the GCs surrounding M87 are consistent with their being an ensemble of test particles (identical in this regard to the Virgo galaxies) that happen to be orbiting in the potential well defined by both the galaxy and its parent cluster.

6. SUMMARY

We have presented a dynamical analysis of the GC system surrounding M87, the cD galaxy at the dynamical center of the Virgo Cluster. Our database consists of new wide-field imaging in the Washington *C* and *T*₁ filters and radial velocities for 278 GCs taken from the literature or obtained during a dedicated spectroscopic survey conducted with the CFHT. This constitutes the largest sample of radial velocities for pure Population II tracers yet assembled for any external galaxy. A complete description of the database is presented in a companion paper (Hanes et al. 2001).

Surface density profiles measured from our *CT*₁ images reveal the metal-poor GCS to be more spatially extended than the metal-rich population, consistent with earlier findings based on *HST* imaging in the central regions of the galaxy. Beyond a radius of $R \approx 1.5R_e$ (10 kpc), the metal-poor clusters dominate the total GCS. The combined, metal-poor and metal-rich samples all show significant rotation of mean amplitude $\Omega R \approx 170 \text{ km s}^{-1}$ about axes whose position angles are indistinguishable from that of the photometric minor axis, $\Theta_0 = 65^\circ$. The metal-rich GCS shows a roughly flat rotation curve of mean amplitude

$\Omega R = 160_{-99}^{+130}$ km s⁻¹. Apart from a possible drift in position angle of the rotation axis at $R \sim 2R_e$, the metal-rich clusters appear to be rotating everywhere about the photometric minor axis of the galaxy. The rotation field, however, appears noncylindrical: a two-dimensional map of the rotation field for the metal-rich GCs shows a “double-lobed” pattern, with maxima at $R \sim 3.5R_e - 4R_e$ (25–30 kpc) along the approximate photometric major axis of the galaxy.

While the mean rotation velocity of the metal-poor GCS, $\Omega R = 172_{-108}^{+51}$ km s⁻¹, is indistinguishable from that of its metal-rich counterpart, a two-dimensional map of the rotation field suggests that this system may rotate as a solid body or, alternatively, it may exhibit a “shear” in the line-of-sight velocity. This putative shear is similar to that observed for Virgo galaxies within 2° of M87, broadly consistent with a scenario in which some, or all, of the distant, metal-poor GCs are gradually infalling onto M87 along Virgo’s principal axis. Inside $R \simeq 2.5R_e$ (18 kpc), the approximate onset of the galaxy’s cD envelope, the metal-poor GCS appears to rotate around the photometric major axis.

The surface brightness profile of M87 has been combined with *ROSAT* observations of the surrounding X-ray gas to construct a mass model for the Virgo Cluster. A comparison of the observed and predicted GC velocity dispersion profiles based on this model and on the measured GC density profiles suggests that the velocity ellipsoid of the composite GCS is almost perfectly isotropic. Dividing the sample on the basis of metallicity reveals the metal-poor clusters to be slightly biased to tangential orbits, with $\beta_{cl} \simeq -0.4$, while

the metal-rich cluster system shows a radial bias of roughly the same magnitude: $\beta_{cl} \simeq 0.4$. We note that a simple mass model for M87 and Virgo provides a remarkably accurate match to the observed GC kinematics, suggesting that the GCs, as a whole, belong to both M87 and the surrounding Virgo Cluster. More detailed conclusions concerning the formation of M87 and its GCS must await the measurement of precise ages for the metal-poor and metal-rich GC systems, the most outstanding observational constraints bearing on this issue.

P. C. gratefully acknowledges support provided by the Sherman M. Fairchild Foundation during the course of this work. D. E. M. acknowledges support from NASA through grant HF-1097.01-97A awarded by the Space Telescope Science Institute, which is operated by the Association of Universities for Research in Astronomy, Inc., for NASA under contract NAS5-26555. D. G. acknowledges financial support for this project received from CONICYT through Fondecyt grant 8000002 and by the Universidad de Concepcion through research grant 99.011.025-1.0. The research of D. A. H. and G. L. H. is supported through grants from the Natural Sciences and Engineering Research Council of Canada. D. A. H. is pleased to thank the Directors of the Dominion Astrophysical Observatory and the Anglo-Australian Observatory for their hospitality and support during a research sabbatical. This research has made use of the NASA/IPAC Extragalactic Database (NED), which is operated by the Jet Propulsion Laboratory, California Institute of Technology, under contract with the National Aeronautics and Space Administration.

REFERENCES

- Arnaboldi, M., et al. 1996, *ApJ*, 472, 145
 Arnaboldi, M., Freeman, K. C., Gerhard, O., Matthis, M., Kudritzki, R. P., Méndez, R. H., Capaccioli, M., & Ford, H. C. 1998, *ApJ*, 507, 759
 Arp, H. 1968, *PASP*, 80, 129
 Ashman, K. M., & Zepf, S. E. 1992, *ApJ*, 384, 50
 Bahcall, J. N., & Soneira, R. M. 1981, *ApJS*, 47, 357
 Barnes, J. 1992, *ApJ*, 393, 484
 Barnes, J., & Efstathiou, G. 1987, *ApJ*, 319, 575
 Barnes, J., & Hernquist, L. 1996, *ApJ*, 471, 115
 Beers, T. C., Flynn, K., & Gebhardt, K. 1990, *AJ*, 100, 32
 Bender, R., Saglia, R. P., & Gerhard, O. E. 1994, *MNRAS*, 269, 785
 Binggeli, B. 1999, in *The Radio Galaxy Messier 87, Ringberg Workshop*, ed. H.-J. Röser & K. Meisenheimer (Berlin: Springer), 9
 Binggeli, B., Popescu, C. C., & Tammann, G. A. 1993, *A&AS*, 98, 275
 Binggeli, B., Sandage, A. R., & Tammann, G. A. 1985, *AJ*, 90, 1681
 Binney, J., & Tremaine, S. 1987, in *Galactic Dynamics* (Princeton: Princeton Univ. Press), 640
 Carlberg, R. G. 1986, *ApJ*, 310, 593
 Carter, D., & Dixon, K. L. 1978, *AJ*, 83, 574
 Cohen, J. G. 2000, *AJ*, 119, 162
 Cohen, J. G., Blakeslee, J. P., & Ryzhov, A. 1998, *ApJ*, 496, 808
 Cohen, J. G., & Ryzhov, A. 1997, *ApJ*, 486, 230
 Côté, P. 1999, *AJ*, 118, 406
 Côté, P., Marzke, R. O., & West, M. J. 1998, *ApJ*, 501, 554
 Côté, P., Marzke, R. O., West, M. J., & Minniti, D. 2000, *ApJ*, 533, 869
 Davies, R. L., & Birkinshaw, M. 1988, *ApJS*, 68, 409
 de Vaucouleurs, G., & Nieto, J.-L. 1978, *ApJ*, 220, 449
 Dubinski, J. 1998, *ApJ*, 502, 141
 Efstathiou, G., & Jones, B. J. T. 1979, *MNRAS*, 186, 133
 Fabian, A. C., Nulsen, P. E. J., & Canizares, C. R. 1984, *Nature*, 310, 733
 Fall, S. M. 1979, *Rev. Mod. Phys.*, 51, 21
 Ferguson, H. C., & Binggeli, B. 1994, *A&A Rev.*, 6, 67
 Ferrarese, L., et al. 1996, *ApJ*, 464, 568
 Fillmore, J. A. 1986, *AJ*, 91, 1096
 Franx, M., Illingworth, G., & de Zeeuw, T. 1991, *ApJ*, 383, 112
 Frenk, C. S., White, S. D. M., Davis, M., & Efstathiou, G. 1988, *ApJ*, 327, 507
 Gebhardt, K., Pryor, C., Williams, T. B., & Hesser, J. E. 1995, *AJ*, 110, 1699
 Geisler, D., & Forte, J. C. 1990, *AJ*, 350, L5
 Geisler, D., Lee, M. G., & Kim, E. 1996, *AJ*, 111, 1529
 Girardi, M., Fadda, D., Giuricin, G., Mardirossian, M., Mezzetti, M., & Biviano, A. 1996, *ApJ*, 457, 61
 Hanes, D. A., Côté, P., Bridges, T. J., McLaughlin, D. E., Geisler, D., Harris, G. L. H., Hesser, J. E., & Lee, M. G. 2001, *ApJ*, in press (Paper I)
 Harris, W. E., Harris, G. L. H., & McLaughlin, D. E. 1998, *AJ*, 115, 1801
 Harris, W. E., & Pudritz, R. E. 1994, *ApJ*, 429, 177
 Hernquist, L. 1992, *ApJ*, 400, 460
 ———. 1993, *ApJ*, 409, 548
 Heyl, J. S., Hernquist, L., & Spergel, D. N. 1996, *ApJ*, 463, 69
 Huchra, J., & Brodie, J. 1987, *AJ*, 93, 779
 Hui, X., Ford, H. C., Freeman, K. C., & Dopita, M. A. 1995, *ApJ*, 449, 592
 Kissler-Patig, M., & Gebhardt, K. 1998, *AJ*, 116, 2237
 Kissler-Patig, M., Grillmair, C. J., Meylan, G., Brodie, J. P., Minniti, D., & Goudfrooij, P. 1999, *AJ*, 117, 1206
 Kundu, A., Whitmore, B. C., Sparks, W. B., Macchetto, F. D., Zepf, S. E., & Ashman, K. M. 1999, *ApJ*, 513, 733
 Lauer, T. R., & Kormendy, J. 1986, *ApJ*, 303, 1
 McLaughlin, D. E. 1995, *AJ*, 109, 2034
 ———. 1999a, *ApJ*, 512, L9
 ———. 1999b, *AJ*, 117, 2398
 ———. 2000, in *ESA SP-445, Star Formation from the Small to the Large Scale*, ed. F. Favata, A. Kaas, & A. Wilson (Noordwijk: ESA), 77
 McLaughlin, D. E., Harris, W. E., & Hanes, D. A. 1993, *ApJ*, 409, L45
 ———. 1994, *ApJ*, 422, 486
 Merritt, D., Meylan, G., & Mayor, M. 1997, *AJ*, 114, 1074
 Merritt, D., & Oh, S.-P. 1997, *AJ*, 113, 1279
 Merritt, D., & Tremblay, B. 1993, *AJ*, 106, 2229
 Mihos, J. C., & Hernquist, L. 1994, *ApJ*, 437, L47
 Mould, J. R., Oke, J. B., de Zeeuw, P. T., & Nemeč, J. 1990, *AJ*, 99, 1823
 Mould, J. R., Oke, J. B., & Nemeč, J. 1987, *AJ*, 93, 53
 Murali, C., & Weinberg, M. D. 1997, *MNRAS*, 291, 717
 Navarro, J. F., Frenk, C. S., & White, S. D. M. 1997, *ApJ*, 490, 493
 Neilsen, E. H., Tsvetanov, Z. I., & Ford, H. C. 1999, in *The Radio Galaxy Messier 87, Ringberg Workshop*, ed. H.-J. Röser & K. Meisenheimer (Berlin: Springer), 50
 Nulsen, P. E. J., & Böhringer, H. 1995, *MNRAS*, 274, 1093
 Ostriker, J. P., Binney, J., & Saha, P. 1989, *MNRAS*, 241, 849
 Peebles, P. J. E. 1969, *ApJ*, 155, 393
 Pesce, E., Capuzzo-Dolcetta, R., & Vietri, M. 1992, *MNRAS*, 254, 466
 Pierce, M. J., Welch, D. L., McClure, R. D., van den Bergh, S., Racine, R., & Stetson, P. B. 1994, *Nature*, 371, 385
 Quinn, P. J., & Zurek, W. H. 1988, *ApJ*, 331, 1
 Ratnatunga, K. U., & Bahcall, J. N. 1985, *ApJS*, 59, 63
 Romanowsky, A. J., & Kochanek, C. S. 2001, *ApJ*, 553, 722

- Schlegel, D. J., Finkbeiner, D. P., & Davis, M. 1998, *ApJ*, 500, 525
Schombert, J. M. 1988, *ApJ*, 328, 475
Schweizer, F. 1980, *ApJ*, 237, 303
Secker, J., Geisler, D., McLaughlin, D. E., & Harris, W. E. 1995, *AJ*, 109, 1019
Sharples, R. M., Zepf, S. E., Bridges, T. J., Hanes, D. A., Carter, D., Ashman, K. M., & Geisler, D. 1998, *AJ*, 115, 2337
Strom, S. E., Strom, K. M., Wells, D. C., Forte, J. C., Smith, M. G., & Harris, W. E. 1981, *ApJ*, 245, 416
Tonry, J. L. 1987, in *IAU Symp. 117, The Structure and Dynamics of Elliptical Galaxies*, ed. T. de Zeeuw (Dordrecht: Reidel), 89
van der Marel, R. P. 1991, *MNRAS*, 253, 710
———. 1994, *MNRAS*, 270, 271
Wahba, G. 1990, *Spline Models for Observational Data* (Philadelphia: SIAM)
Warren, M. S., Quinn, P. J., Salmon, J. K., & Zurek, W. H. 1992, *ApJ*, 399, 405
Weil, M. L., Bland-Hawthorn, J., & Malin, D. F. 1997, *ApJ*, 490, 664
Weil, M. L., & Hernquist, L. 1994, *ApJ*, 431, L79
———. 1996, *ApJ*, 460, 101
West, M. J. 1993, *MNRAS*, 265, 755
West, M. J., & Blakeslee, J. P. 2000, *ApJ*, 543, L27
West, M. J., Côté, P., Jones, C., Forman, W., & Marzke, R. O. 1995, *ApJ*, 453, L77
White, R. E. 1987, *MNRAS*, 227, 185
White, S. D. M. 1982, in *Morphology and Dynamics of Galaxies, Twelfth Advanced Course of the Swiss Society of Astronomy and Astrophysics*, ed. L. Martinet & M. Mayor (Geneva: Geneva Obs.), 291
Whitmore, B. C., Sparks, W. B., Lucas, R. A., Macchetto, F. D., & Biretta, J. A. 1995, *ApJ*, 454, 73
Zepf, S. E., & Ashman, K. M. 1993, *MNRAS*, 264, 611
Zepf, S. E., Beasley, M. A., Bridges, T. J., Hanes, D. A., Sharples, R. M., Ashman, K. M., & Geisler, D. 2000, *AJ*, 120, 2928